


WATER-IN-AIR DROPLET FORMATION IN PLASMA BONDED  
MICROCHANNELS FABRICATED  
BY SHRINKY-DINK LITHOGRAPHY

By

Christopher J. Bender Jr.

RECOMMENDED:

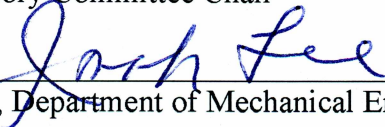
  
\_\_\_\_\_

  
\_\_\_\_\_

  
\_\_\_\_\_

  
\_\_\_\_\_

Advisory Committee Chair


  
\_\_\_\_\_

Chair, Department of Mechanical Engineering

APPROVED:

  
\_\_\_\_\_

Dean, College of Engineering and Mines

  
\_\_\_\_\_

Dean of Graduate School

  
\_\_\_\_\_

Date

WATER-IN-AIR DROPLET FORMATION IN PLASMA BONDED  
MICROCHANNELS FABRICATED  
BY SHRINKY DINKS® LITHOGRAPHY

A  
THESIS

Presented to the Faculty  
of the University of Alaska Fairbanks

in Partial Fulfillment of the Requirements  
for the Degree of

MASTER OF SCIENCE

By

Christopher J. Bender Jr., B.S.

Fairbanks, Alaska

August 2011

## Abstract

This thesis presents the first work on water-in-air droplet microfluidics. Polymeric microchannels were prototyped to illustrate water droplet formation in air by the T-junction mediated design. The first part of the thesis is on the proof of using unfiltered air as the process gas for plasma-assisted bonding of polydimethylsiloxane (PDMS) microchannels. A series of bilayered PDMS prototypes were plasma bonded under various plasma treatment parameters to determine the optimal settings for high-strength bonding. Pressure rupture tests were conducted to measure the bonding interface strength, which were shown to be as high as 135 psi. The second part of the thesis illustrates the formation and dispersion of water droplets in a continuous air flow in microchannels, and discusses the mechanisms of how droplets are formed. The Shrinky Dinks® lithography and plasma-assisted bonding were used to prototype leakage-free microchannels for testing droplet production. Droplets are formed under the competition between the fluid viscosity and surface tension forces. The channel dimensions and the fluid flow rates dictate the mechanism of droplet formation. The major finding is that the droplet length increases and droplet velocity decreases with increasing water flow rates, but some droplets were not formed at the T-junction. These findings are discussed

## Table of Contents

Signature Page.....	i
Title Page.....	ii
Abstract.....	iii
Table of Contents.....	iv
List of Figures.....	vii
List of Tables.....	xii
Acknowledgements.....	xiii
Chapter 1 Introduction and Overview.....	1
1.1 Microfluidics.....	1
1.2 Droplet Microfluidics.....	1
1.3 Motivation, Objectives & Structure of Thesis.....	2
Chapter 2 Unfiltered Air Plasma Assisted Bonding.....	4
2.1 Bonding Overview and Literature Review.....	4
2.2 Method 1 -- Non-Permanent Adhesion Bonding.....	6
2.3 Method 2 -- Less Cross-Linking Agent.....	7
2.4 Method 3 -- Partial Curing.....	8
2.5 Method 4 -- Stamp-and-Stick.....	8

2.6	Method 5 -- Hand-Held Corona Discharge .....	9
2.7	Method 6 -- Plasma Oxygenation.....	10
2.8	Determining Optimal Bonding Procedure.....	11
2.9	Chapter Conclusion .....	26
Chapter 3	Air Sheared Liquid Microdroplets in T-Junction.....	28
3.1	Introduction .....	28
3.2	Liquid-Liquid Droplet Formation .....	28
3.3	Gas-Liquid Bubble Formation .....	31
3.4	Liquid-in-Gas Droplet Formation .....	32
3.5	Principle of Droplet Formation by Shearing.....	33
3.6	Channel Fabrication .....	34
Chapter 4	Experimental Procedure.....	36
4.1	Fabrication.....	36
4.2	Apparatus and Analysis.....	42
Chapter 5	Results & Discussion .....	50
5.1	Droplet Length Results.....	50
5.2	Length versus Water Flow Rate .....	50
5.3	Droplet Velocity Results .....	58

5.4	Droplet Formation Mechanisms.....	63
5.5	Chapter Conclusions .....	70
Chapter 6	Summaries and Future Work .....	72
6.1	Summaries of Chapter Conclusions.....	72
6.2	Future Work .....	73
References	.....	75

## List of Figures

Figure 1: Sylgard 184 Silicon Elastomer Kit (Dow Corning Corp., MI) .....	12
Figure 2: My Weigh i201 Digital Scale (My Weigh, British Columbia) .....	13
Figure 3: Fisher Scientific Vacuum Chamber (Thermo Fisher Scientific, MA) .....	13
Figure 4: Harrick Plasma Plasmaflo PDC-FMG & Harrick Plasma Plasma Cleaner PDC-32G (Harrick Plasma NY).....	14
Figure 5: Oerlikon Trivac D2,5E Vacuum Pump (Oerlikon Corp., Switzerland) .....	14
Figure 6: Armitron Stopwatch (Armitron Corp., NY).....	14
Figure 7: Corning PC-620D Hot Plate (Corning Inc., NY) .....	15
Figure 8: Example of Manual Peel Test of Bonded Layers. This image depicts medium RF, 60 second bond time at 300 mTorr bond pressure. The outcome was approximately 40% bonded. ....	15
Figure 9: Press with .023" hole punch creating probe inlet .....	19
Figure 10: Dremel Model 200 with 1/32" Drill Bit (Robert Bosch Tool Corp., IL) .....	19
Figure 11: Seal-It Adhesive Backed Vinyl Tape (LePage 2000 Inc., MI) .....	19
Figure 12: 0.025in Outer Diameter Stainless Steel Round-Tip Probe (itronx, Inc., CA). 20	
Figure 13: CAD drawing of two-layered PDMS-PDMS test subject with stainless steel probe in air inlet .....	20
Figure 14: Craftsman Air Compressor model 919-167320 (KCD IP, LLC., IL) .....	21
Figure 15: Bond Test Setup. The pressure transducer was plugged into a multimeter which read 1 psi for 1mV.....	21

Figure 16: Comparison of variations in controlled variables and the effect on the rupture pressure .....	24
Figure 17: Depiction of EWOD operation. K. Hosokawa et al, Anal Chem. 71, 4781-4785, (1999). The electrode introduces electricity to the droplet, temporarily altering its interfacial energy(left). Electricity can also be used to propel droplets (right). .....	31
Figure 18: Shear focusing, Lecture notes prepared by Cheng-fu Chen, University of Alaska Fairbanks. ....	34
Figure 19: Offset channel curve at the channel where fluid is introduced into the device to aid in droplet breakup. ....	37
Figure 20: CAD drawing of design to be used. The perpendicular inlet is 10mm long. The vertical paths are 20mm long. The radius of curvature is 5mm. The inlets have a 10mm diameter. ....	38
Figure 21: Channels Printed on thermalplastic sheet.....	39
Figure 22: Comparison of mold before & after baking. ....	39
Figure 23: A large vacuum is used to eliminate the air bubbles that are created when the PDMS mixture is stirred and poured in the container. ....	39
Figure 24: Cut the cured PDMS sheet out using a sharp razor. ....	40
Figure 25:Drill press with 1/32: bit creating inlet holes. ....	40
Figure 26:Cleaning of the surfaces using tape produces a cost effective means of pre-surface cleaning. It can be done multiple times to ensure a debris free surface. ....	40



Figure 27: Insert the shelf with care. The barrel inside is plastic and can be scratched. Ensure the surfaces to be bonded are facing up. ....	40
Figure 28: Adjustment of pressure is done by turning the knob attached to the chamber cap clockwise to reduce the pressure and counterclockwise to increase the pressure. ....	41
Figure 29: With air plasma, the color emitted is purple. It is important to not over expose the PDMS or damage to the molecular backbone can be done. ....	41
Figure 30: Preheat hotplate to 80°C. ....	42
Figure 31: Test setup schematic. ....	43
Figure 32: Testing setup. Fastcam-PCI R2 Highspeed Camera recorded the droplets through an Accu-Scope 3030 Inverted Microscope. The device was fed by 2 syringe pumps. ....	44
Figure 33: Schematic of droplet velocity calculation. ....	45
Figure 34: Depiction of velocity calculation where L is the length of the viewing window, A is the initial frame, B is the ending frame, and duration of each frame is 0.001s. ....	46
Figure 35: Location of viewing window. ....	46
Figure 36: Cut of 1.5pt line width channel. The cross sectional area and perimeter were measured using AutoCAD area toolbar. $A_c = 11289\mu\text{m}^2$ $P = 619\mu\text{m}$ . ....	48
Figure 37: Cut of 1.25pt line width channel. The cross sectional area and perimeter were measured using AutoCAD area toolbar. $A_c = 9909\mu\text{m}^2$ $P = 591\mu\text{m}$ . ....	48
Figure 38: Cut of 1pt line width channel. The cross sectional area and perimeter were measured using AutoCAD area toolbar. $A_c = 8520\mu\text{m}^2$ $P = 548\mu\text{m}$ . ....	49

Figure 39: Droplet length versus water flow rate. The pt size refers to the line width printed onto the thermalplastic sheet. 1.5pt has a channel width of 292 $\mu$ m, 1.25pt is 281 $\mu$ m, and 1pt is 258 $\mu$ m. ....	52
Figure 40: Average droplet length versus water flow rate in the 1.5pt line width is depicted. One standard deviation of each average is incorporated into the graph. ....	53
Figure 41: Average droplet length vs water flow rate in the 1.25pt line width is depicted. One standard deviation of each average is incorporated into the graph. ....	54
Figure 42: Average droplet length vs water flow rate in the 1pt line width is depicted. One standard deviation of each average is incorporated into the graph. ....	55
Figure 43: Droplet velocity versus water flow rate. The pt. size refers to the line width printed onto the thermalplastic sheet. 1.5pt has a channel width of 292 $\mu$ m, 1.25pt is 281 $\mu$ m, and 1pt is 258 $\mu$ m. ....	59
Figure 44: Example of consecutive droplets in dry channel. The droplets have the same length and velocities. ....	62
Figure 45: Example of consecutive droplets in wet channel. The droplets lengths and velocities differ. ....	62
Figure 46: Picture taken at 25x DIN LWD plan achromat objective, N.A. 0.40, W.D. 4.8mm. ....	64

Figure 47: Droplet formation at T-Junction. Top Left: droplet forming from water "tail." Top Right: Droplet interfacial stresses overtaking viscosity stresses. Bottom Left: Initial separation of droplet from water tail. Bottom right: Droplet separation from water tail. (The light gray area indicates the water phase, and the area with brighter dots is occupied by air). .....	65
Figure 48: $Q_L=4 \mu\text{L}/\text{min}$ , $Q_G=120 \mu\text{L}/\text{min}$ in a 1.5pt linewidth channel. The water and air have become stratified. Left: Viewing window. Right: T-junction. ....	66
Figure 49: Droplet formation at the outlet. ....	68
Figure 50: Droplet formed in outlet. This picture is of the outlet hose with a droplet traveling through it.....	69
Figure 51: Water accumulation creating droplets approximately 3000 $\mu\text{m}$ from T-junction flowing right to left. Left: Water accumulation. Right: Droplet being formed from water accumulation on water tail when pressure becomes great enough to shear it. The product leaves the water tail. ....	69

**List of Tables**

Table 1: RF Level LO (6.8W) 300mTorr Chamber Pressure .....	16
Table 2: RF Level MED (10.5W) 300mTorr Chamber Pressure.....	16
Table 3: RF Level HI (18W) 300mTorr Chamber Pressure .....	16
Table 4: RF Level LO (6.8W) 200mTorr Chamber Pressure .....	17
Table 5: RF Level MED (10.5W) 200mTorr Chamber Pressure.....	17
Table 6: RF Level HI (18W) 200mTorr Chamber Pressure .....	17
Table 7: Rupture pressure results for controlled variables in air plasma showering .....	23
Table 8: Droplet length versus liquid flow rate .....	56

## **Acknowledgements**

The author would like to thank Dr. Cheng-fu Chen for his continued advice and support as the committee chair and undergraduate advisor, and committee members Dr. Horacio Toniolo, Dr. Tom Green, and Dr. Jifeng Peng for their guidance. Thanks also goes to the SMART scholarship for the payment of tuition and included stipend for three and a half years, as well as a career in the Department of Defense after graduation and the Institute of Northern Engineering office for an assistantship position and Alaska NASA EPSCoR Program for support in purchasing the equipment. The author would also like to thank his family and friends for their encouragement through the years. Finally, the author would like to thank his fiancé Nichole Renee Campiglia for all her love and support and for a lifetime of happiness.

## **Chapter 1 Introduction and Overview**

### **1.1 Microfluidics**

Since its introduction over decades ago, microfluidics has been increasingly studied in numerous multidisciplinary fields. This relatively new technology implements milliliter to nanoliter volumes of fluid in diverse fields such as chemistry and biology to electrical and bioengineering. Applications in microfluidics range from microreactors to metabolism and toxicology screenings. By using such a minute volume of reagents, reaction times are drastically reduced and only a fraction of the lab space is required (Teh, 2008).

Microfluidic channels have been manufactured using photolithography, soft lithography, and more recently, Shrinky Dinks®. Photolithography proves to be a costly and time consuming method of creating channels in thin silicon and silicon dioxide disks. Soft lithography utilizes some of the same methods as photolithography, but does not require such expensive and brittle components, and can use polydimethylsiloxane (PDMS) as a substrate. Shrinky Dinks® are a form of soft lithography, but are mere children's toys, which greatly cut costs of expensive silicon and silicon dioxide. These methods of channel fabrication will be further discussed in Chapter 3.

### **1.2 Droplet Microfluidics**

A subcategory of microfluidics, droplet microfluidics uses discrete volumes of immiscible fluids. This variance from continuous flow systems enables performance of

large numbers of reactions without increasing the devices size, quantity, or complexity. Recent studies have discovered that droplet microfluidic systems can perform simple Boolean logic functions, a monumental step towards the development of a microfluidic chip (Fuerstman, 2007; Cheow, 2007; Gershenfeld, 2007).

Microfluidics involves manipulation of miniscule volumes of fluids in microdevices in essentially laminar flow, yielding low Reynold's numbers. Droplet microfluidics includes generation of these minute volumes in discrete, monodispersed droplets at rates as high as 20,000 per second with diameters as low as 45nm (Teh, 2008). The large surface area to small volume enables fast reaction times and reduced time for heat transfer as well as shorter distances for diffusion.

Microdevices for droplet generation have been manufactured from assorted polymers. A large number of microfluidic devices are created from PDMS, an inexpensive, elastomeric polymer that is easily moldable. This material has a high transparency and is hydrophobic. Methods such as plasma exposure have been found to temporarily turn the surface of PDMS hydrophilic, easing microfluidic filling of channels (Tang, 2006).

### **1.3 Motivation, Objectives & Structure of Thesis**

Significant effort has been given towards development of microfluidic systems in PDMS devices using oxygen plasma assisted bonding. Devices implementing liquid-liquid emulsions have been well studied since the immersion of droplet microfluidics in PDMS devices. Gas-in-liquid systems are a more recent development, employing gas plugs in a liquid carrying fluid. The testing of liquid-in-gas systems, however, has not been

investigated. With gas being the carrier fluid at high flow rates, strong bonds between two-layered PDMS devices must exist to endure high pressures. Using pure oxygen requires added complexity of setup and enhanced costs as does photolithography as a microchannel fabrication method.

The objective of this thesis is to create water droplets in a continuous air carrier fluid in two-layered PDMS microfluidic devices fabricated from Shrinky Dinks® soft lithography and ensure that rupturing at the bonded surface does not occur. A T-junction channel geometry was chosen for droplet shearing.

In the following chapters, literature reviews of bonding and microfluidics will be conducted. A bond rupturing test of varying unfiltered air assisted plasma parameters will be investigated to find the optimal parameters for high strength PDMS-PDMS bonding. The manufacturing of nine microfluidic devices using Shrinky Dinks® to create a master mold of the T-junction serpentine channels will then be discussed. There will be three channel widths with three devices per width tested with a constant air flow rate with increasing water flow rate. The average lengths and average velocities of the droplets are recorded and discussed, as well as the dynamics and properties of droplet production taking place. The paper will conclude with suggestions for future work.



## Chapter 2 Unfiltered Air Plasma Assisted Bonding

### 2.1 Bonding Overview and Literature Review

In our studies the fluid flow is operated in enclosed microchannels. In order for proper fluid flow through the elastomer device, it is required that all the PDMS layers be bonded appropriately to prevent fluid leakage. A poor bond will lead to device rupture during operation of fluids in microchannels when an external pressure is applied to the fluid (Tang, 2006). This chapter is devoted to developing a proper procedure for bonding along with numerous tests of the bonding strength, as well as reviewing other bonding techniques.

A few important factors must be considered when developing bonding methods to seal microchannels made of PDMS. This polymeric elastomer consists of a silicone resin solution mixed with a cross-linking agent composed of dimethyl, methylhydrogen siloxane typically in a 10:1 ratio (Dow Corning Corporation, 2011). It is a commonly used material in the microfluidic field because it is relatively inexpensive, easily moldable, and can be rapidly produced (Teh, 2008), and is optically transparent down to a wavelength of 280 nm (Tang, 2006). PDMS also has a high gas permeability which gives it similar features of a plethora of biological and cellular applications (Tang, 2006). PDMS is naturally hydrophobic, but when cleaned with plasma the surface temporarily converts to hydrophilic. This is due to the oxidation of the surface silicone molecules, creating silanol group (-OH) from the original  $-\text{O}-\text{Si}(\text{CH}_3)_2-$  chain. The channel walls become negatively charged when the neutral and basic aqueous solutions are introduced.

This property supports electroosmotic pumping allowing high surface energy liquids (primarily water) to easily fill the channels (Duffy, 1998). When two plasma cleaned substrates are pressed together, they create a permanent covalent bond (Si-O-Si).

Because of its adhesive nature, PDMS can also be temporarily bonded by simply pressing two cured (or partially cured) substrates together. The temporary bonding can be repeated numerous times. The bond strength is significantly less in a temporary versus permanent bond, which will be discussed later.

Strength of the bond is critical in pressurized devices such as when compressed gases are utilized (Eddings, 2008). Size requirements of the device can also be a limiting factor in methodology. Some forms of bonding require limited space, which can inhibit the size of the manufactured device (Haubert, 2006). In industry, reproducibility and volume are pertinent aspects to be considered (van Midwoud, 2010), and cost is a driving factor that is sought to be minimized (Harris, 2007; Haubert, 2006). Complexity of the design can be a contributing factor to how bonding is carried out (Chueh, 2007; Tan, 2005). Surface chemistry is another concern in the biomedical applications (Teh, 2008), which also demand a see-through devices. The cleanliness of the environment where the fabrication takes place, and the preparation and curing of the PDMS, together, with the previously mentioned factors, all collectively affects the bonding strength.

In the following sections, six common methods will be discussed. Temporary bonding such as the pressing together mentioned above will be evaluated as well as permanent bonding, including: cross-linking agent manipulation, partial curing of substrates, the

stamp-and-stick method, the hand-held corona discharge method, and plasma oxygenation. These methods were compared in a parallel study by (Eddings, 2008). Further research was conducted for the purpose of this study to obtain an easily reproducible, strong, and rapid means of bonding that will be implemented for water-in-air droplet formation.

This chapter will also seek to discourage notions that plasma bonding produced inconsistencies in rupture pressure in induction coupled barrel reactors (Plasma & Plasma Cleaning, n.d.). By altering vacuum chamber pressure, exposure time, and radio frequency, constant reproducibility was achieved, with rupture pressures exceeding test equipment capability (135 psi, 930kPa).

## **2.2 Method 1 -- Non-Permanent Adhesion Bonding**

The simplest method considered in this literature is the standard non-permanent adhesion. This employs two (or more) 10:1 PDMS substrates. All that is required in this method is a scale to assure the right mixture, a container for the PDMS, and an oven for curing. The mixture is cured in the shape of its container. The two devices are then cut out and bonded by simply pressing them together. As previously mentioned, the PDMS material has properties that make it mildly adhesive after curing. (Eddings, 2008) tested the bond strength of non-permanent bonding and compared it to other bond strategies. They inject compressed air into a cavity that is fabricated and bonded in two PDMS layers. The air pressure was guided to the cavity using a hard compressed airline with a pressure gauge. The devices were bonded and put into a soap and water solution so that if leakage

occurred it would be plainly visible to the naked eye. The pressure was increased incrementally until signs of bubbles became evident. It shows that the non-permanent bonding has an average bond strength of 160 kPa (1.58 atm).

### **2.3 Method 2 -- Less Cross-Linking Agent**

In the formation of making the PDMS devices, a cross-linking agent is mixed with the PDMS base. A common practice of preparing PDMS is to use a 10:1 ratio for the base to agent mixture due to the hardness and stickiness of the result (Dow Corning Corporation, 2011). Besides this common practice, other trials have attempted using a higher ratio for bonding, which is to reduce the use of the cross-linking agent (Eddings, 2008; Duffy, 1998). Therefore, this method is to appropriately employ the nature of the material to adhere to an object. The reduction in the cross-linking agent leads to a softer, sometimes tacky, cured PDMS piece. The procedure for this method requires materials and procedure as Method 1 (Eddings, 2008).

In the bond strength test of (Eddings, 2008), the rupture pressure was on the order of 365-517 kPa (3.61-5.12 atm) with an optimized ratio of 15:1 and an average of 474 kPa (4.69 atm). This shows higher bond strength in results versus Method 1. The cost is reduced by not requiring special equipment that is required in the plasma bonding. The sticky cured PDMS pieces are harder to handle and thus could have adverse results for some applications.

Manipulation of the mixture ratio proves to be a simple, cheap, effective and reproducible means of bonding according to (Eddings, 2008). It was found that the surfaces remained

hydrophobic, requiring more force to generate fluid filling in the channels). The high bond strength comes with the price of requiring more force, which is undesirable because the micro-channels may be collapsed by pressing the PDMS pieces too hard.

#### **2.4 Method 3 -- Partial Curing**

Partial curing retains the favored 10:1 ratio of the substrate for biomedical applications. Instead of using post-curing properties for removable adhesion, adhesion before full curing ensures permanent bonding. In this method, the PDMS is semi-cured and then stacked together for full curing. This bonding method will produce a solid single piece with imbedded microchannels. The second curing usually takes 10-35 minutes under an elevated temperature. No special equipment is needed. This method yields high bond strengths from 390-690 kPa (3.86-6.83 atm) versus the previous methods (Eddings, 2008).

This type of bonding has a high variability due how precisely timed the PDMS layers must be stacked. The short window of time limits optimal bonding and introduces bubbles and submerged channels as well as lack of permanent bonding. (Middelstat, 2010) shows that timing is critical and minor changes can drastically alter effectiveness. It is to also be noted that the channel surface remains hydrophobic in this bonding process.

#### **2.5 Method 4 -- Stamp-and-Stick**

The stamp-and-stick method (Eddings, 2008) implements a technique that has been proven to have many benefits in certain applications. A small amount of uncured 10:1

cross-linking agent is applied to the surface of one cured PDMS piece to act as an adhesive. The other cured PDMS that is to be bonded is stacked to the first piece. The stack is then exposed to UV light or baked in an oven. The sandwiched cross-linking agent will then create a permanent bond between the two pieces after the glue layer is cured. This method proved to be one of the strongest in the (Eddings, 2008) study (545-690 kPa or 5.39-6.83 atm) and the most reproducible. There is no need for an excessively clean environment, or expensive machinery. It is a flexible bonding procedure for requiring little lead time of preparation. It is suggested that this bonding method would be best applied for multilayer devices with adequate clearance around the channels for application of the adhesive cross-linking agent.

One major drawback of this method is that a good alignment skill is needed when stacking two to-be-bonded pieces after applying the adhesive. Due to its low viscosity, the cross-linking agent has a tendency to diffuse readily and could flush the microchannel patterns on the to-be-bonded pieces. Minute amounts only need to be applied; therefore this is best suited for devices with large bondable areas. Because no oxidation takes effect on the substrate surfaces, the channels remain hydrophobic and can impinge on possible designs.

## **2.6 Method 5 -- Hand-Held Corona Discharge**

Corona discharge is a simple, portable form of bonding that acts much like plasma oxygenation without the heavy costs. This method (Haubert, 2006; Eddings, 2008) uses a hand-held device that emits a strong voltage potential between the electrodes that ionizes

air above the PDMS surface. It does not require extreme cleanliness or a vacuum chamber. The distance between the electrodes can be adjusted or interchanged to accommodate the size and shape of the object. (Haubert, 2006) used a BD20-AC hand-held corona treater. This study altered the contact angles for optimization which ranged from  $92^\circ$  to  $105^\circ$ . Without having to vacuum out a chamber, the time of production could be reduced to 10-15 seconds per piece.

(Eddings, 2008) tested a hand-held corona discharge device and found that it had the lowest bond strength 227-380 kPa (2.45-3.76 atm), but had a slightly lower standard deviation of 8.9. This shows that the results are more reproducible and less time consuming than the plasma oxygenation, but had less bond strength.

## **2.7 Method 6 -- Plasma Oxygenation**

Plasma oxygenating has been a favored method for bonding since its introduction in 1998 by (Duffy, 1998). When applying a plasma around the PDMS, the atomic structure becomes altered, exposing silanol groups (-OH) for a limited time from a  $\text{O-Si}(\text{CH}_3)_2$  form (Tang, 2006). When the silanol exposed surface comes into contact with another silanol exposed surface, a covalent siloxane (Si-O-Si) bonds permanently. This temporary atomic structure alteration also converts the surface from hydrophobic to hydrophilic, easing fluid filling through the channels of the PDMS.

This method requires a vacuum chamber that can permit low pressures under 300mTorr in some trials and under 100mTorr in others. The environment must be clean to eliminate debris contamination which will negatively affect the bonding. It only takes 10-40

seconds of oxygen plasma shower to produce the needed silanol groups (-OH) for bonding (Tang, 2006; Eddings, 2008; White, 2007). This method requires an expensive plasma cleaner, however. It was also observed that the oxygen plasma produces inconsistent results (Eddings, 2008). In the same conditions, the shear strength of the PDMS ranged from 180 kPa to 715 kPa (1.78-7.08 atm) with a standard deviation of 13.4 kPa. The oxygen plasma approach also requires speed and delicacy to avoid bonding errors that were commonly encountered in this study. Due to the availability of this equipment, the turnover time of samples, and the hydrophilic surface product, plasma oxygenation was chosen to be the primary bonding approach used in this thesis. To set our work different from the already established, we studied the feasibility of using unfiltered air as the process gas for the plasma-assisted bonding. In the following section we elaborate this approach in detail together with the tests of bonding strength.

## **2.8 Determining Optimal Bonding Procedure**

With the numerous studies tried with drastic differences in controlled variables for plasma surface cleaning, twenty-four trials were run in this study by altering three control variables to determine the optimal configuration for this application. The control variables were: power applied to radio frequency (RF) coil that is used to produce the air plasma, pressure level in the vacuum chamber of the plasma cleaner, and time of exposing the PDMS pieces during oxygen plasma shower. Temperature was held constant in the testing room at 20°C. Air was the gas used in the chamber



The samples under the bonding strength test were created from the same blend and container so as to limit the chance of variability in the mixture. The PDMS was poured into a 9"x9"x2" aluminum container 0.17" deep (5mm) and baked at 200°F for 8 minutes. Pieces were then cut out in 1"x1" squares and put on a glass shelf, two at a time with bonding surfaces up, which is in turn placed into the plasma cleaner. The next steps will describe the materials used and a breakdown of the manufacturing procedure.

Various equipment was used in finding the optimal bonding methodology. Creating the two-layered PDMS devices required Dow Corning Corp. (MI) Sylgard 184 silicon elastomer kit, a My Weigh (British Columbia) i201 Digital Scale, and a Thermo-Fisher Scientific (MA) vacuum chamber (Figure 1, Figure 2 and Figure 3).



**Figure 1: Sylgard 184 Silicon Elastomer Kit (Dow Corning Corp., MI)**

Dow Corning Elastomer kit contains a silicon resin solution and a cross-linking agent.



**Figure 2: My Weigh i201 Digital Scale (My Weigh, British Columbia)**

The mixture is created using 10:1 by weight resin to cross-linking agent.



**Figure 3: Fisher Scientific Vacuum Chamber (Thermo Fisher Scientific, MA)**

The mixture is then poured into an aluminum container with a glass slide at the bottom up to 5mm thick and degassed in a vacuum chamber. Once it is degassed, it is cured in an oven for 8 minutes at 200°F.

A variety of machines were required to perform plasma bonding. These include: a Harrick Plasma (NY) Plasmaflo PDC-FMG and Plasma Cleaner PDC-32G, an Oerlikon Corp. (Switzerland) Trivac D2,5E vacuum pump, an Armitron Corp. (NY) stopwatch, and a Corning Inc. (NY) PC-620D hot plate (Figure 4-Figure 7).



**Figure 4: Harrick Plasma Plasmaflo PDC-FMG & Harrick Plasma Plasma Cleaner PDC-32G (Harrick Plasma NY)**

After debris removal, the sheets are put on a glass shelf and inserted into the plasma cleaning device. The machine parameters of chamber pressure and power are adjusted before turning on the cleaner (Harrick Plasma, n.d.).



**Figure 5: Oerlikon Trivac D2,5E Vacuum Pump (Oerlikon Corp., Switzerland)**

The vacuum pump is attached to the cleaner and PlasmaFlo assembly. It is controlled using the vacuum chamber cover.



**Figure 6: Armitron Stopwatch (Armitron Corp., NY)**

The stop watch is used to control the exposure time of the PDMS sheets in the plasma cleaner. After the desired time has passed, the sheets are removed from the plasma cleaner.



**Figure 7: Corning PC-620D Hot Plate (Corning Inc., NY)**

Once removed from the plasma cleaner the sheets are stacked. The devices were then put on a hotplate at 80°C and pressed together to evacuate all air bubbles for 10 minutes.

The bond strength was tested by two steps. The first step is rough, and was done by manually pulling the pieces apart and assessed on approximately what percent permanently bonded together. Prototypes that were perfectly bonded or at least 90 percent were re-tested manually to ensure reproducibility. See Table 1 through Table 6 for test results. Figure 8 shows an example of a two-layered PDMS-PDMS test subject undergoing a manual peel to determine bonded surface percentage.

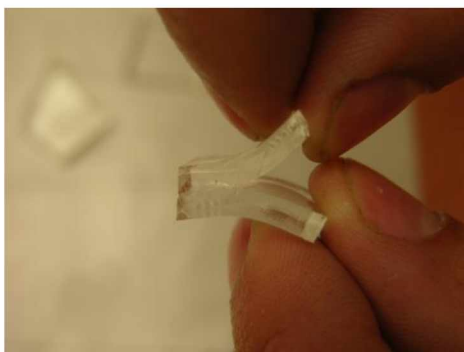


**Figure 8: Example of Manual Peel Test of Bonded Layers. This image depicts medium RF, 60 second bond time at 300 mTorr bond pressure. The outcome was approximately 40% bonded.**

It should be noted that 15 seconds for 200 mTorr chamber pressure and 18 seconds for 300 mTorr chamber for the plasma to become present is not incorporated into these

times. Plasma formation becomes evident when a purple light is emitted out of the plasma cleaner.

**Table 1: RF Level LO (6.8W) 300mTorr Chamber Pressure**

Time (sec)	% Bonded
30	90
40	90
50	95
60	100

**Table 2: RF Level MED (10.5W) 300mTorr Chamber Pressure**

Time (sec)	% Bonded
30	95
40	80
50	70
60	40

**Table 3: RF Level HI (18W) 300mTorr Chamber Pressure**

Time (sec)	% Bonded
30	60
40	0
50	0
60	60

**Table 4: RF Level LO (6.8W) 200mTorr Chamber Pressure**

Time (sec)	% Bonded
30	100
40	100
50	80
60	100

**Table 5: RF Level MED (10.5W) 200mTorr Chamber Pressure**

Time (sec)	% Bonded
30	100
40	100
50	40
60	90

**Table 6: RF Level HI (18W) 200mTorr Chamber Pressure**

Time (sec)	% Bonded
30	80
40	30
50	20
60	10

The bonds that achieved 90% or greater continued to the next trial. The test samples were remanufactured to nullify any excess separation that may occur during peeling. The second trial consisted of a compressed air injection system. The subjects were created using the same steps as for the first test, but additional manufacturing was required for air injection. Eleven of the squares were hole punched using the press MHPM-UNV with 0.023" hole punch, see Figure 9 (Schmidt, PA) and drilled 1mm deep using a 1/32" drill bit fixed to a Dremel® Model 200 (Robert Bosch Tool Corporation, Germany) depicted in Figure 10, cleaned using Seal-It® adhesive backed vinyl tape (LePage's 2000 Inc., MI) depicted in Figure 11. A blank PDMS square and a hole punched square were then placed on the glass shelf, face up, and bonded. Following (Eddings, 2008), air was released into the bonded surface by a metal probe attached to an air compressor and was inserted directly into the center of the PDMS stack (Figure 12 and Figure 13). The stack was then inserted into a cup of soap and water solution so that rupturing of the bond would be evident by the bubbles. The pressure from the Craftsman Air Compressor model 919-167320 (KCD IP, LLC., IL) in Figure 14 was measured using a Fluke pressure transducer (Tequipment Net, NJ) attached to a Fluke multimeter (Tequipment Net, NJ). The hose fittings were sealed using CFPC 1/2"x5/20" Teflon Thread Seal Tape and connected by Watts A-730 Pipe Tee 0.25" FIP and Watts A-729 Hex Nipple 0.25" MIP (Watts, MA) with a 1/32" hole drilled into the nipple where the plastic hosing was epoxied (see Figure 15). The following steps show the additional procedure for the second bond strength trial.

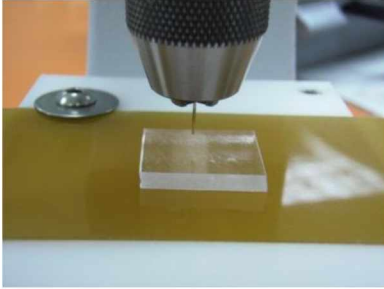


**Figure 9: Press with .023" hole punch creating probe inlet**

The PDMS substrate is then cut out of the container and one to-be-bonded substrate is hole punched using a 0.023" punch in the center of the sheet.



**Figure 10: Dremel Model 200 with 1/32" Drill Bit (Robert Bosch Tool Corp., IL)**

A pressure chamber is then drilled 1mm deep into the punched hole using a 1/32" drill bit.



**Figure 11: Seal-It Adhesive Backed Vinyl Tape (LePage 2000 Inc., MI)**

Adhesive backed vinyl tape is used to clean the surfaces of the hole punched sheet and a plain sheet of PDMS. This proves to be a cheap method of removing debris.





**Figure 12: 0.025in Outer Diameter Stainless Steel Round-Tip Probe (itronx, Inc., CA)**

After the device was on the hotplate for 10 minutes, stainless steel probes were inserted into the punched hole down to the top of the drilled pressure chamber.

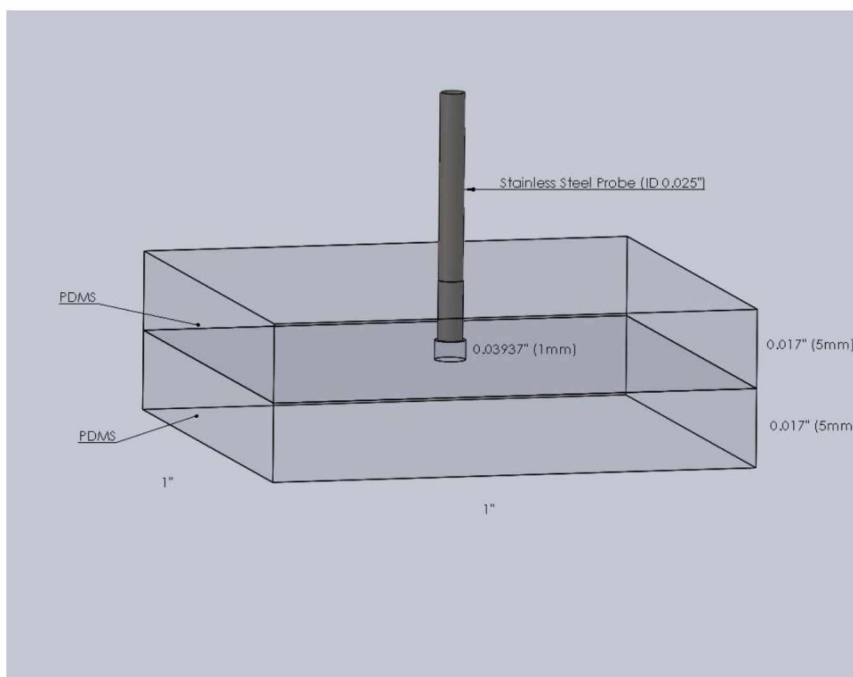


**Figure 13: CAD drawing of two-layered PDMS-PDMS test subject with stainless steel probe in air inlet**



**Figure 14: Craftsman Air Compressor model 919-167320 (KCD IP, LLC., IL)**

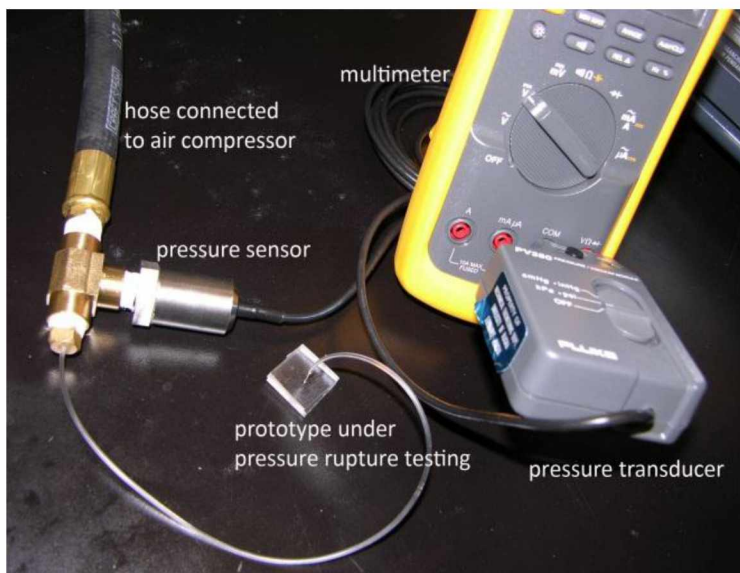


**Figure 15: Bond Test Setup. The pressure transducer was plugged into a multimeter which read 1 psi for 1mV.**

The test results can be seen in Table 7 and Figure 16. It should be noted that the air compressor used has a pressure capacity up to 135 psi. Rupture pressures at 135 psi shown in the table indicates that the bonding strength exceeds 135 psi. To put ensured failure modes in as a comparison, times of 10 seconds and 90 seconds at varying chamber pressure and power were implemented.

**Table 7: Rupture pressure results for controlled variables in air plasma showering**

Power (W)	Pressure (mTorr)	Time (sec)	Pressure <sub>Bond</sub> (mTorr)	Bond Time (sec)	Pressure <sub>Rupture</sub> (psi)	Pressure <sub>Rupture</sub> (kPa)
LO (6.8)	300	10	300	10	127	876
LO (6.8)	300	30	300	30	110	758
LO (6.8)	300	40	300	40	135	931
LO (6.8)	300	50	300	50	135	931
LO (6.8)	300	60	300	60	135	931
LO (6.8)	300	90	300	90	127	876
MED (10.5)	300	10	300	10	110	758
MED (10.5)	300	30	300	30	135	931
MED (10.5)	300	90	300	90	127	876
HI (18)	300	10	300	10	127	876
HI (18)	300	90	300	90	127	876
LO (6.8)	200	10	200	10	15	103
LO (6.8)	200	30	200	30	105	724
LO (6.8)	200	40	200	40	90	621
LO (6.8)	200	60	200	60	105	724
LO (6.8)	200	90	200	90	5	34
MED (10.5)	200	10	200	10	25	172
MED (10.5)	200	30	200	30	135	931
MED (10.5)	200	40	200	40	135	931
MED (10.5)	200	60	200	60	135	931
MED (10.5)	200	90	200	90	40	276
HI (18)	200	10	200	10	5	34
HI(18)	200	90	200	90	95	655

It shows that medium power applied to the RF coil (10.5W) had the most occurring rupture pressure exceeding the capabilities of the air compressor, as highlighted in the

table. The samples with 300 mTorr bond pressure did not have 100% bonded surface area in the first trial. The MED 200 mTorr at 30 seconds and 40 seconds both did.

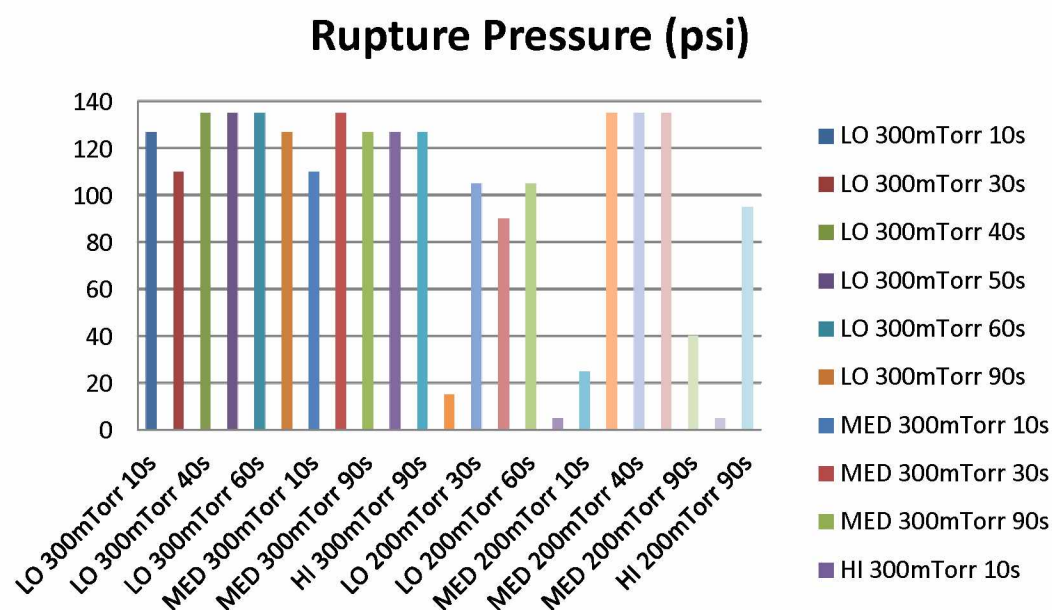


**Figure 16: Comparison of variations in controlled variables and the effect on the rupture pressure**

Figure 16 gives a visual idea of the comparative failures occurred based on slight modifications to time, pressure and power input. For droplet testing with microchannels in the PDMS layers, 30 second bonds at medium RF (10.5W) and a chamber pressure of 200mTorr was used to reduce time. There was never any bonding leaking that occurred during this study with these chosen bonding criteria.

To further emphasize the reproducibility of the chosen bond, ten two-layered PDMS bonded devices were created using the chosen criteria showing repeatable results with no technical flaw. The results showed that all 10 of the test subjects exceeded the rupture pressure that could be outputted by the air compressor (135 psi, or 930 kPa). It was noted

in (Eddings, 2008) that the plasma bonding produces drastic variability with bonds rupturing from 180 kPa to 715 kPa as per the device production procedure of (Bhattacharya, 2005). The chamber pressure was high compared to those tested in this thesis (700 mTorr). The power and time were similar, however, at 20W and 30 seconds.

A major issue that occurred during testing was surface cracking initiated upon insertion of the stainless steel probe. To prevent air leakage out of the insertion hole, 10:1 PDMS mixture was applied around the inlet and cured in an stovetop convection oven at 200 °F (93°C) for 8 minutes after the probe was inserted. This insured sealing of the fractures.

There were two failure modes that occurred in the second test. One was a common problem leakage around the metal probe. The two failing apparatus' were dried using a paper towel and 10:1 PDMS was reapplied around the probe. The prominent failure mode was separation of the bonded surfaces do to the introduced pressure.

An improvement that is suggested in replication of this study is different injection techniques. The stainless steel probes with rounded tips ruptured the surface at every instance of insertion. Using beveled tipped probes reduces the initial cross-sectional area being inserted, and may then reduce cracking. It was also found that directly inserting the plastic tubing into the PDMS with a 45° cut tip reduced fracturing. The flexibility of both the PDMS device and the plastic hosing limit the shear stress introduced by the rigid stainless steel probes.

An additional improvement that can be taken into account is temperature variations in the plasma chamber. This showed no obvious effects when 100 °C was compared to samples

at 150° (Tang, 2006); however, it may reduce the amount of time required in the chamber due to easier formation of plasma.

## **2.9 Chapter Conclusion**

Twenty four samples were created using two-layered PDMS substrates to test the bonding strength by air plasma, which is governed by three control variables: the time, RF (power input), and vacuum chamber pressure were all altered to determine the optimal combination of these variables for further testing in microdroplet formation. The first trial was subjected to a manual peel test to identify the percentage of the surface was bonded. All surfaces that were 90% bonded and above were remanufactured and subjected to an air injection testing until the bond failed. Several samples outlasted the pressure input from the air compressor, from which we suggest the following set-up of the control variables of the plasma chamber for optimal PDMS bonding.

Due to the peeling test and time reduction being an optimal variable, optimal bonding for the proceeding tests will be with 30 second bond time (with an added 15 second plasma warm up time) at medium (10.5W) radio frequency, and 200mTorr chamber pressure.

After further testing with the optimal bonding variables, it was noticed that 10 two-layered plasma bonded PDMS substrates withstood 135 psi (930 kPa) of compressed air being injected into the bonded surface. The withstood capacity is significantly greater than reviewed in the previous sections. This demonstrates that plasma bonded PDMS to PDMS devices can be reproducible with no variation in bond strength in induction coupled barrel reactors as previously suspected (Eddings, 2008) and that bond strengths

in excess of 930 kPa are attainable by air plasma bonded two-layered PDMS-PDMS devices.



## **Chapter 3 Air Sheared Liquid Microdroplets in T-Junction**

### **3.1 Introduction**

Droplet formation in microchannels has been increasingly investigated since the initialization over two decades ago (Manz, 1990). Microfluidics has played a key role in many chemical and bioengineering fields due to the small volume required to undergo chemical reactions as well as the ability for micro in-vitro testing (Teh, 2008; van Midwoud, 2010; Brouzes, 2009; Drew, 2004). This field has many promises for future multidisciplinary studies with the utilization of reduced quantities of reagents in drastically reduced reaction times.

Studies of droplet production have been conducted for immiscible fluids such as water-in-oil droplets, oil-in-water droplets, and air-in-water bubbles. These emulsions use geometric, shear focusing, or electrohydrodynamic (EHD) techniques to guide the immiscible fluids in controlled, repeatable droplet sizes in PDMS devices (Teh, 2008).

### **3.2 Liquid-Liquid Droplet Formation**

Typical liquid-liquid emulsions consist of water-in-oil droplets with oil being the continuous phase fluid and water being the dispersed phase fluid. The formation of droplets in the continuous fluid from the dispersed fluid is dictated by many controlling factors. Viscosity of the fluids, as well as the miscibility, interfacial tension, channel surface, and velocity can facilitate the size and production rate of the droplets (Baroud, 2004). Velocity of the continuous fluid plays a critical role in droplet formation. Water miscible fluids (e.g., glycerol) can be added to reduce viscosity, therefore increasing the

interfacial tension between the two fluids allow for easier shearing. Higher viscosities will also increase interfacial tension (Tan, 2009) which can be used for oil. Surfactants have been used to convert hydrophobic channels to hydrophilic, or vice-versa depending on the requirements. This can favor formation of oil droplets or water droplets. An increased carrying fluid velocity has been shown to increase droplet production rate (Yobas, 2006).

Droplet formation can be more quantitatively determined by the capillary number, which is dimensionless and defined as:

$$Ca = \mu V / \gamma, \quad \text{Eq. (1)}$$

where  $\mu$  is the dynamic viscosity,  $V$  is the velocity of the fluid to be broken up into droplets, and  $\gamma$  is the interfacial tension of the two fluids. The capillary number is a ratio of the shear stress (viscous stress) to surface tension. During droplet formation, there is a tug of war between the viscosity and the surface tension -- the stronger the viscosity is, the harder the continuous flow is to break up. If the surface tension is stronger, then we expect a breakup of the continuous flow and thus droplets are formed. A critical capillary number determines when droplet break-off will occur for liquid-liquid droplet formation. It is essential for the channel surface to be completely wetted by the continuous fluid to eliminate dispersed fluid surface adhesion (Baroud, 2004). Droplets in this state are called “plugs” and are fully encased in the continuous phase fluid. The elimination of channel contact will prevent the plug from adsorbing to the channel, which can disrupt the reproducibility of the droplets. (Dreyfus, 2003) showed that partial wall wetting of

both fluids in a systematic study reduced the reproducibility of droplet formation and the fluid interfaces took on an irregular shape. The fluids also adsorbed in many locations of the channel.

Droplets can be manipulated by passive methods such as geometry-mediated techniques and viscosity alterations, and active methods such as the electrohydrodynamic (EHD) based techniques. Geometry considerations include: T-junction intersections, cross-junction intersections, and flow focusing. This topic will be further discussed later. As mentioned above, water-miscible fluids (such as glycerol) can be mixed with water to reduce viscosity thereby increasing the interfacial tension. The EHD methods such as the electrowetting on dielectrics (EWOD) change the interfacial energy using electricity depicted in Figure 17. The interfacial tension influences the contact angle; therefore introducing electricity can cause the fluid to wet the surface creating a temporary hydrophilic surface. The imbalanced surface tension force drives the droplet to move.

Liquid-in-liquid droplet production has been thoroughly studied with variations in physical properties. Geometric techniques allow for droplet shearing at a chosen point. Careful design of channel geometries can facilitate droplet formation, size control, and the production rate.

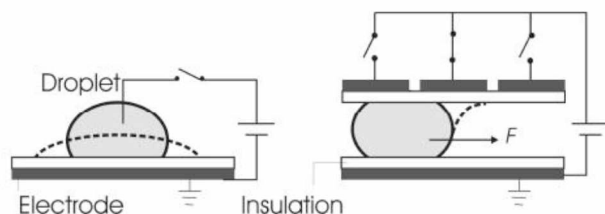


**Figure 17: Depiction of EWOD operation. K. Hosokawa et al, *Anal Chem.* 71, 4781-4785, (1999). The electrode introduces electricity to the droplet, temporarily altering its interfacial energy(left). Electricity can also be used to propel droplets (right).**

Adjustments of flow rates can also increase droplet production by surpassing the critical capillary number in droplet shearing techniques. Water additives, such as glycerol, are common to reduce viscosity and increase interfacial tension between water and oil. Other interfacial tension techniques such as EWOD are implemented to selectively create hydrophilic surfaces in microchannels to form and move droplets. Many of these methods are also used in more recent droplet microfluidics studies.

### 3.3 Gas-Liquid Bubble Formation

Gas-in-liquid bubble formation is an emerging topic in the study of droplet microfluidics. This topic consists of liquid as a continuous phase and gas as the dispersed phase. When the gas flows at a low rate, a foam-like flow regime is created at lower flow rates, while plugs are formed at higher flow rates (Baroud, 2004). At even higher gas flow rates, a “slug-annular regime” can be observed, in which bubbles are encased in the continuous liquid phase film. As the gas flow rate increases further, liquid adheres to the channel walls and the gas flows between the liquid films in an annular structure (Triplett, 1999).

In a study conducted by (Tan, 2009), a series of gas plugs in a water/glycerol solution were created and tested at various liquid and gas flow rates. The solution varied from 0% glycerol to 15, 24, 30, and 35%. Tween 20 was used as the surfactant. A T-junction channel was milled into a sheet of polymethylacrylate (PMMA), which was pressure sealed to another sheet, and tested at varying angles of injection of the liquid phase. The gas phase was directed in-line with the channel direction, while the liquid phase was directed at 60°, 90°, and 120° to the gas phase flow. It was observed that the plug length could be estimated using the formula:

$$\frac{L}{w} = \frac{1}{2} \left( \frac{Q_d}{Q_c} \right)^{1/2} Ca^{-1/5} \quad \text{Eq. (2)}$$

where  $L$  is the gas plug length,  $w$  the channel width,  $Q_d$  is the gas flow rate,  $Q_c$  the liquid flow rate, and  $Ca$  is the capillary number. The paper does not, however, take in to account droplets without the use of a surfactant. (Tan, 2009) also plotted the dispersed phase length versus the dispersed phase flow rate. Their study shows that the higher the viscosity the higher the dispersed phase length.

### 3.4 Liquid-in-Gas Droplet Formation

This thesis focused on the formation of liquid droplets in a continuous gas phase. This type of droplet formation can be particularly useful when discrete quantities of liquid are required with separation of gas to eliminate back pressure effects, such as in syringes (Chen, 2008). Problems have arisen in the area of bioengineering where reduced cross-sectional areas of cannula increase backpressure. It was observed in (Chen, 2008) that

reducing the channel diameter 10-fold exhibited a 100-fold times larger back pressure in continuous flows. The application of liquid-in-gas can potentially reduce this problem.

The formation of monodispersed water-in-air was investigated to determine the droplet size, production rate, and velocity versus the variable injected flow rate with a constant gas flow rate. T-junction channels were used with varying channel dimensions in plasma bonded PDMS. Testing followed the procedures of (Tan, 2009). A variation in the injection criteria was implemented. By convention, the continuous phase is injected perpendicular to the channel and the dispersed phase is introduced in line with the channel, while the opposite was done in this thesis. Reasons for this will be discussed in the following section.

### **3.5 Principle of Droplet Formation by Shearing**

The flow focusing techniques have been widely studied in microdroplet production to yield monodispersed segments of fluid. In terms of the T-junction, a focused fluid is sheared by a perpendicular focusing fluid (see Figure 18). The breakup of the droplets at the intersection is dependent on the viscous forces and the interfacial tension between the two mediums. This effect is termed the Rayleigh-Plateau instability, which states that the instability of the focused fluid is due to pressure instability inside the liquid caused by minute deviations in the local curvature. The fluid seeks to obtain the lowest surface energy, causing it to break into cylindrical droplets once the capillarity has reached a critical value. The local shear occurs when the interfacial tension overcomes the viscous stresses. The focused fluid will then separate at a given point and form a droplet.

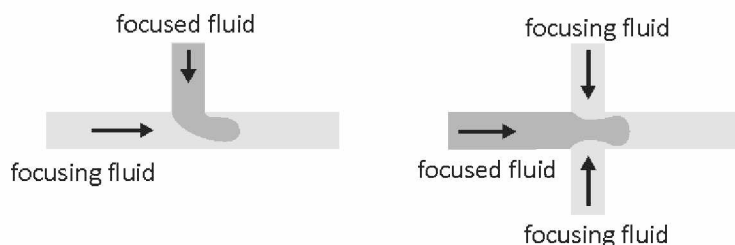


**Figure 18: Shear focusing, Lecture notes prepared by Cheng-fu Chen, University of Alaska Fairbanks.**

### 3.6 Channel Fabrication

Photolithography has been termed the ‘gold standard’ for microfabrication and microfluidic device creation (Grimes, 2008). This process has been able to make semiconductors that are 29 nm and were mass produced by TSMC and IBM in 2007 (Chen, 2010). Photolithography creates designs on silicon wafers. The wafers are chemically cleaned, rinsed in distilled water baths and dried. They are then cleaned using oxygen plasma. A photo resist is then spin-coated and baked to harden. A photolithography machine is then used to imprint the designed photoresist onto the silicon wafer using an illumination passing through a reticle and then a concentrating lens. This process must all take place in a clean room and is very cost prohibiting. The silicon wafers are also very brittle.

Another method of microchannel fabrication is soft lithography. This method was developed by Whitesides’ group at Harvard University (Chen, 2010) and uses an elastomeric stamp or mold to transfer patterns to the substrate. Unlike the silicon wafers, these polymeric materials are flexible. This method has been shown to produce features down to 30  $\mu\text{m}$  (Xia, 1998) and can be used on common microfluidic substrates such as

PDMS and PMMA. Soft lithography is done by creating a negative master mold out of silicon dioxide, silicon nitride, or various metals using photolithography and pouring the polymer over the master mold and allowing it to cure. Each master mold can be used to fabricate more than 50 PDMS replicas according to (Xia, 1998).



## Chapter 4 Experimental Procedure

### 4.1 Fabrication

Shrinky Dinks® lithography is a relatively new means of microchannel manufacturing that implements a children's toy to create polymeric master molds that PDMS can be poured onto creating channels as small as 65  $\mu\text{m}$  wide (Grimes, 2008). This fabrication method was used to prototype the microfluidics for this thesis' experimental work.

Shrinky Dinks® lithography is a cost effective method which uses thermalplastic sheets to prepare mold masters for replication. Shrinky Dinks® is trademark for polystyrene sheets that shrink approximately 63% when baked and are primarily used as adolescent's toys (K & B Innovations, 2010). Channel designs can be created in a CAD program and printed onto the thermalplastic sheets using 1200+ dpi. It was observed by (Xia, 1998) that the surface feature height can increase by up to 500% when baked at a uniform temperature of 163°C for 3-5 minutes. Using Shrinky Dinks® is a form of soft lithography, but without the use of expensive photolithography created master molds. The channels can easily transport large mammalian cells (>10  $\mu\text{m}$  in diameter). The fabrication of two-layered PDMS to PDMS devices can be concluded in less than 1 hour. Shrinky Dinks® polystyrene sheets have proven to be a cost effective means of producing microfluidic channels.

The channel design was drawn in a CAD program using a basic serpentine design with a T-junction. The first curve in the design was offset from the first straight segment where the fluids are introduced as seen in Figure 19. The effects of this were not compared to

an aligned channel and should be looked into in future work. The transition reduces the channel width and then increases it immediately afterwards. This is thought to reduce the surface energy, increasing likelihood of droplet separation in cases where fluid wetting has occurred up to this point (Teh, 2008). The idea of offsetting the channel is of my own.

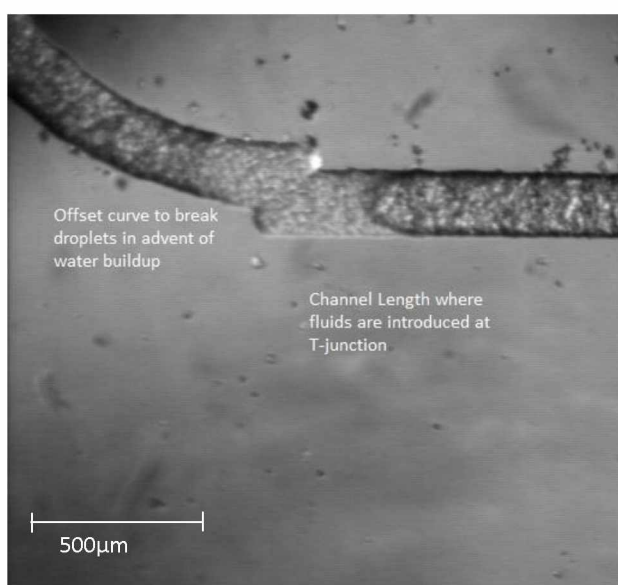
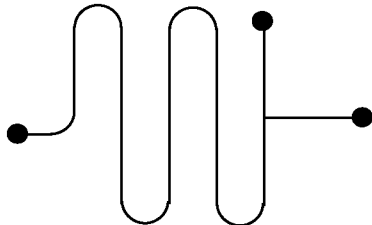


**Figure 19: Offset channel curve at the channel where fluid is introduced into the device to aid in droplet breakup.**

The following procedure is a step-by-step guide to create a two-layered device. Baked thermalplastic sheets were used to create a T-junction, channeled master mold for a two-layered microfluidic device, which was fabricated by plasma bonding two sheets of cured, 10:1, Dow Corning Sylgard 184 silicon elastomer PDMS. Using this process (e.g., see the Fabrication section) here the procedure is first outlined, and then elaboration of each step is given below. Figure 20 shows the geometric channel design used in this

study. Figure 21 is a picture of the channels printed on to a thermalplastic sheet using a 1200 dpi laserjet printer. Figure 22 depicts a side by side comparison of the area shrinkage of the thermal plastic sheet after sufficient heat is applied. The PDMS is degassing in Figure 23. Figure 24 shows a post-cured PDMS substrate being removed from the container encasing the positive mold. Figure 25 is a picture of the inlets being made. Figure 26 is a picture of surface cleaning using adhesive backed tape. Inserting the PDMS substrates into the bonding chamber is shown in Figure 27. The plasma generating device is depicted in Figure 28. An example of the excited atoms due to the plasma is shown in Figure 29. Bonding occurs on the hotplate, which is seen in Figure 30.

A T-Junction design was implemented with 2 inlets and 1 outlet. The design had 3 difference channel widths, 0.35mm, 0.4375mm, and 0.525mm using CAD software. The channel had a slight offset when entering the first curve to enhance droplet shearing.



The designs were printed onto a thermal plastic sheet using 1200 dpi resolution.

**Figure 20: CAD drawing of design to be used. The perpendicular inlet is 10mm long. The vertical paths are 20mm long. The radius of curvature is 5mm. The inlets have a 10mm diameter.**

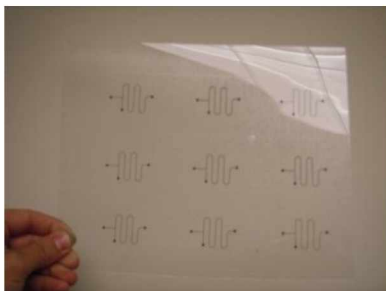


**Figure 21: Channels Printed on thermalplastic sheet.**

The sheets were then cut out leaving adequate space around the channels. The sheets were baked at 235°F for 10 minutes. The size reduction is approximately 62.5% (Franks, 2008). This process compacts the ink creating a protruded surface. Allowing the sheets to completely flatten before removal from oven will

ensure a level molding surface.

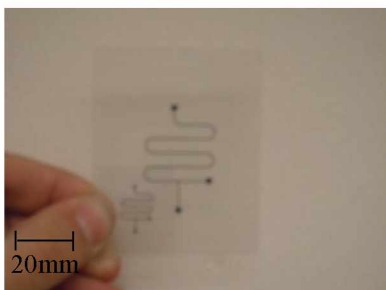


**Figure 22: Comparison of mold before & after baking.**

A 10:1 PDMS mixture (by weight) is then prepared and poured into an aluminum foil container surrounding the thermalplastic mold 5mm deep. It must then be placed into a vacuum to allow degassing.



**Figure 23: A large vacuum is used to eliminate the air bubbles that are created when the PDMS mixture is stirred and poured in the container.**

The PDMS is cured in an oven at 200°F for 10 minutes, allowed to cool to room temperature and then cut out, leaving adequate space around the channels. Blank sheets are also created using the same method, but with a glass slide in an aluminum foil container.



**Figure 24: Cut the cured PDMS sheet out using a sharp razor.**

The channeled sheet is then drilled using a 1/32" drill through the inlet and outlet.

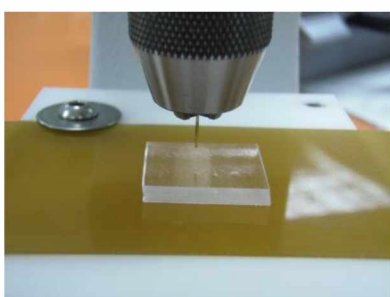


**Figure 25: Drill press with 1/32: bit creating inlet holes.**

The blank and channeled substrates are then laid on the bonding shelf (bonding surface up) and cleaned using Seal-it adhesive backed vinyl tape.

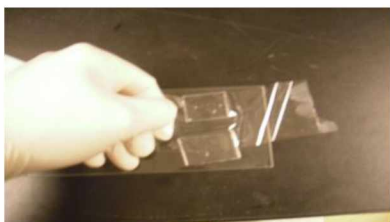


**Figure 26: Cleaning of the surfaces using tape produces a cost effective means of pre-surface cleaning. It can be done multiple times to ensure a debris free surface.**

The shelf is then inserted into the plasma cleaner.

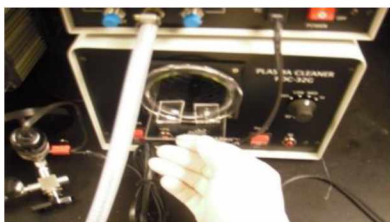


**Figure 27: Insert the shelf with care. The barrel inside is plastic and can be scratched. Ensure the surfaces to be bonded are facing up.**

The chamber is then closed off. The vacuum is turned on and the pressure is adjusted to 200mTorr. Once the pressure has reached this value the plasma power can be set to medium (10.5W) and turned on (RF switch on this model (Harrick Plasma, n.d.)).



**Figure 28: Adjustment of pressure is done by turning the knob attached to the chamber cap clockwise to reduce the pressure and counterclockwise to increase the pressure.**



**Figure 29: With air plasma, the color emitted is purple. It is important to not over expose the PDMS or damage to the molecular backbone can be done.**

The machine will power the coil. Once enough energy has been introduced, the chamber will emit a purple glow for air (between 15 and 19 seconds). Other inert gases may be used as well. Allow the machine to run for 30 seconds with the plasma on.

Immediately shut off the plasma power switch and the vacuum. Remove the shelf and place the blank substrate on the hotplate at 80°C, followed by the channeled substrate. Atmospheric exposure can contaminate the surfaces, reducing bonding. Press them together, ensuring that any air bubbles exist. Care is needed to not collapse the channels. Allow the device to sit for 10 minutes.



**Figure 30: Preheat hotplate to 80°C.**

As mentioned previously, the devices can be created from beginning to end in under an hour. Multiple devices can be created simultaneously. Baking of the thermalplastic sheet without cutting is not advised, as it has a tendency to curl and stick together becoming unusable.

#### **4.2 Apparatus and Analysis**

The device was attached to two syringes. One syringe contained distilled water. The other was filled with air. Both were at 20°C. The syringes were fixed in syringe pumps. A 0.02" ID plastic Tygon tubing (63018-044, VWR Labshop, Batavia, IL) was attached to the syringe needle on one end, and at the other a 45 degree angle was cut and put into the inlet holes of the PDMS device. Figure 31 and Figure 32 show a schematic of the testing setup and an image of the testing setup.

Three channel dimensions (i.e., 1 pt, 1.25 pt, and 1.5 pt, cf. Figure 36, Figure 38, and Figure 37) were tested out for producing droplets at various flow rates of water and air streams which were pumped to meet at the T-junction of the channel.

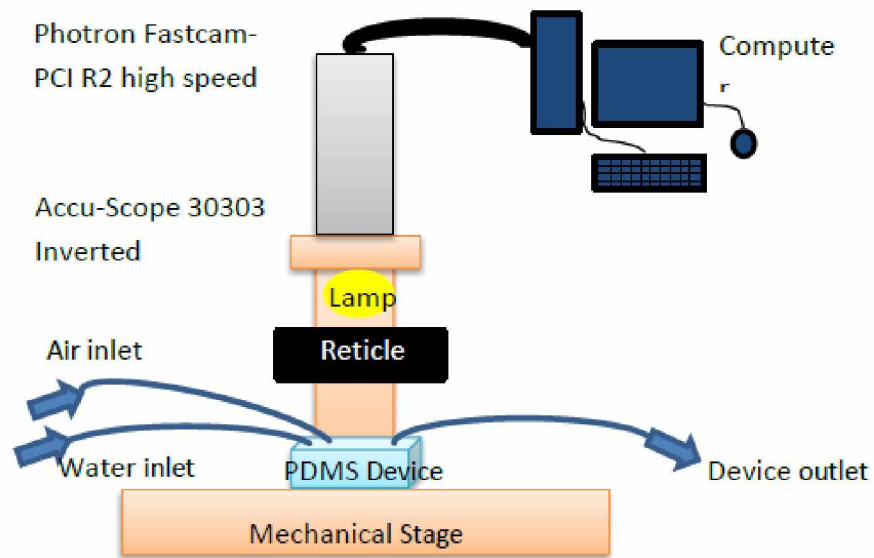
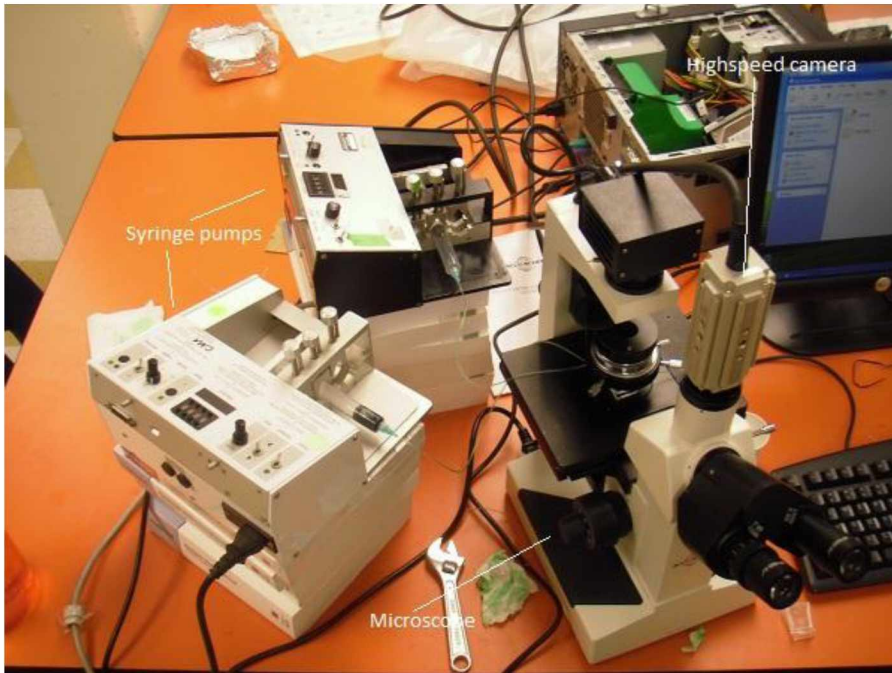


Figure 31: Test setup schematic.





**Figure 32: Testing setup. Fastcam-PCI R2 Highspeed Camera recorded the droplets through an Accu-Scope 3030 Inverted Microscope. The device was fed by 2 syringe pumps.**

The length of the viewing window,  $L$ , of the Photron Fastcam-PCI R2 high-speed camera (Itronx, CA) was measured from using a known width of the channel measured on a Digital Blue USB Connected Digital Microscope (Digital Blue Inc., GA). The high speed camera was fixed to an Accu-Scope 3030 Inverted Microscope (GreatScope, Inc., NC), as shown in Figure 32. The speed of a droplet moving in the channel was estimated by dividing the viewing dimension ( $L$ , see Figure 33) by the time spanned for the droplet to move across the viewing window. The time spanned was in turn calculated per Eq.

(3):

$$V = \frac{L}{(B-A) \cdot \Delta t (\text{s/frame})} \quad \text{Eq. (3)}$$

in which, by referring to Figure 33, A is the frame number when the droplet's leading edge enters the viewing window, B the frame number when the droplet's leading edge exits the window, and  $\Delta t$  is the duration between each frame (e.g., 0.004s, an adjustable parameter of the high-speed camera) as seen in Figure 33.

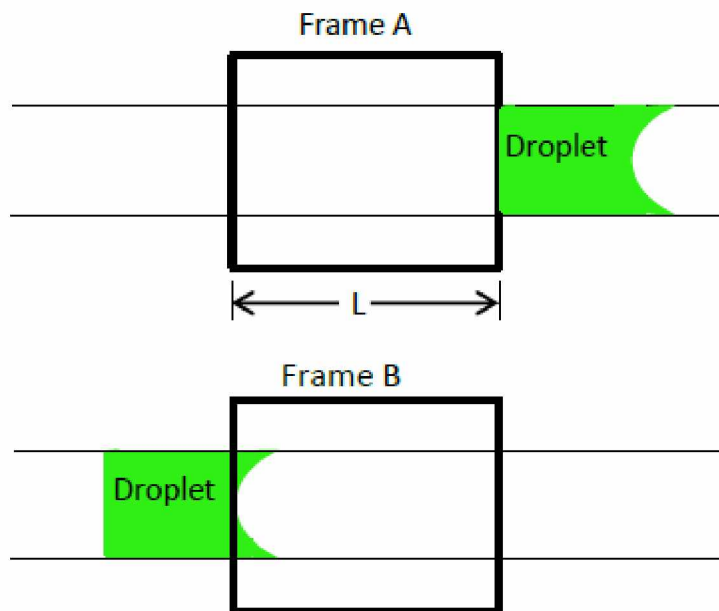


**Figure 33: Schematic of droplet velocity calculation.**

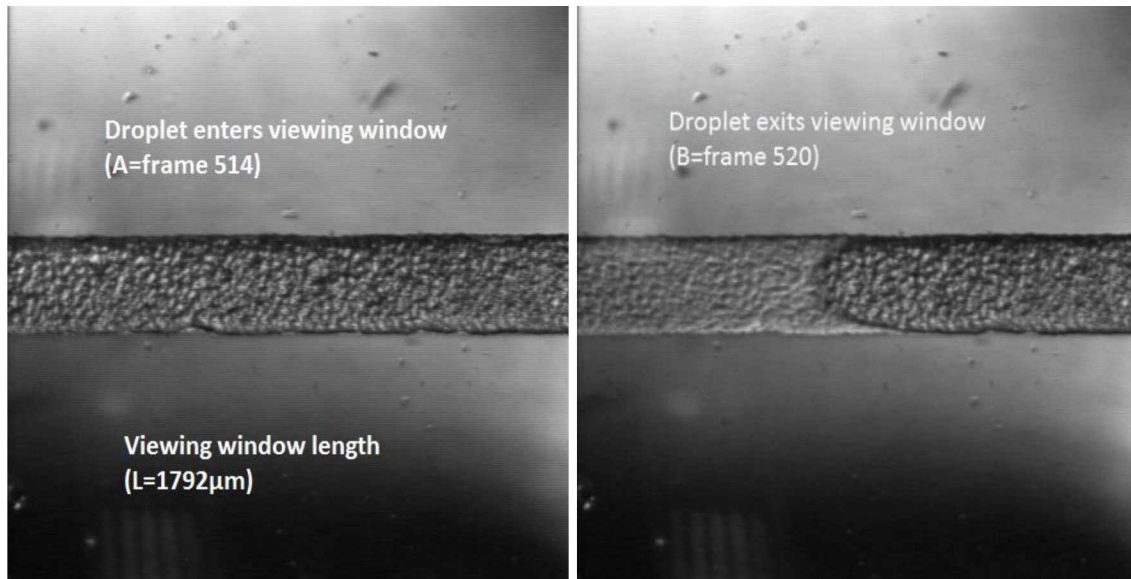


**Figure 34:** Depiction of velocity calculation where  $L$  is the length of the viewing window,  $A$  is the initial frame,  $B$  is the ending frame, and duration of each frame is 0.001s.

The viewing window was placed 25,000 $\mu\text{m}$  down the path of the channel from the T-junction to observe droplets, as seen in Figure 35. Droplets reported longer than 25,000 $\mu\text{m}$  were considered to be continuous flowing water and were thus not included in the later analysis for droplet formation.

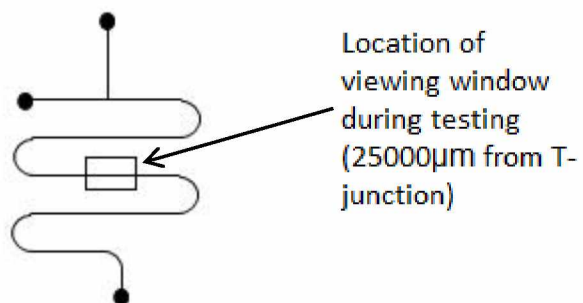


**Figure 35:** Location of viewing window.

The gas flow rate was  $60\mu\text{L}/\text{min}$  herein unless otherwise mentioned. The liquid flow rate was started at  $1\mu\text{L}/\text{min}$  and recorded by the high-speed camera at 250 frames per second for 8.704 seconds (2176 frames) when reaching the memory capacity of the camera. The dimensions of the different channels were calculated by cutting the devices in half and photographing them using the scale on the Digital Blue USB Connected Digital Microscope at 200x zoom. They can be seen in Figure 36, Figure 37 and Figure 38. The images were imported into AutoCAD and using the measurements of the microscope a scale in the program properties. The area tool was used to compute the cross-sectional area of three channels; the widths were measured at the base using the distance tool; the heights of the channels were measured in the center of the cross-section from the base to the top of the channel using the distance tool.

The liquid flow rate was set to  $1\mu\text{L}/\text{min}$  and allowed 10-30 minutes to initially equilibrate. The flow rate was then increased by  $1\mu\text{L}/\text{min}$  and allowed to equilibrate for 100 seconds as per (J. Tan, 2009). I also examined droplet formation that did not occur at the T-junction.

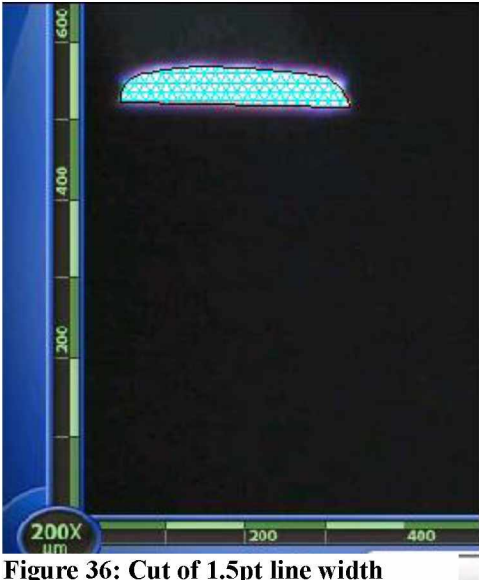


**Figure 36: Cut of 1.5pt line width channel. The cross sectional area and perimeter were measured using AutoCAD area toolbar.  $A_c = 11289\mu\text{m}^2$   
 $P = 619\mu\text{m}$ .**



**Figure 37: Cut of 1.25pt line width channel. The cross sectional area and perimeter were measured using AutoCAD area toolbar.  $A_c = 9909\mu\text{m}^2$   
 $P = 591\mu\text{m}$ .**

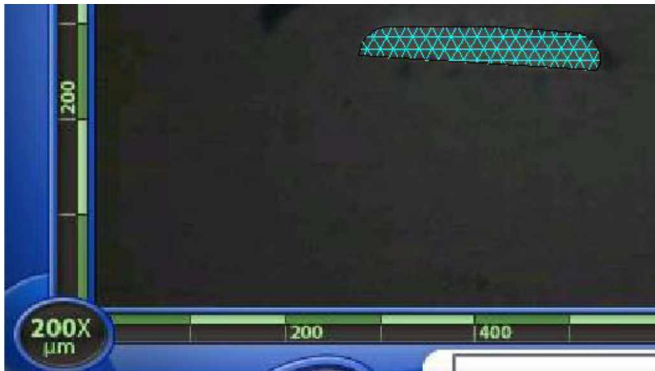


**Figure 38: Cut of 1pt line width channel. The cross sectional area and perimeter were measured using AutoCAD area toolbar.  $A_c = 8520\mu\text{m}^2$   $P = 548\mu\text{m}$ .**

## Chapter 5 Results & Discussion

### 5.1 Droplet Length Results

The droplets can be produced at varying sizes moving at varying speeds, both of which are dictated by the channel geometry as well as the flow rates of the water and air streams at the T-junction. Each prototype was individually tested. After air and water were pumped into the microchannels, the two pressure-driven flows eventually meet at the T-junction, at which the competition between the water viscosity and water-air interfacial tension takes place. Droplets form whenever the interfacial tension dominates the competition so that the continuous water flow is cut off. Small inertial effects compared to large viscous effects yield small Reynold's numbers. When each experiment is initiated, 10-30 minutes usually needs to be allotted before the competition is stabilized for uniform droplet production. Then the high-speed camera begins to record the droplet formation images at the viewing window for up to 8.7004 seconds (which is the memory capacity of the camera).

The droplet velocities and lengths were thus recorded and then averaged according to channel width and water flow rate. Figure 39 shows the results of the droplet lengths. The results took on similar trends as (Tan, 2009), but did not follow their equation. The results are elaborated below.

### 5.2 Length versus Water Flow Rate

Arbitrary water flow rate cannot always produce droplets. The range of the water flow rates were constrained by when droplets were no longer produced and the fluids became

stratified as described in (Baroud, 2004). Droplets in the line width of 1.5pt were able to be formed at all water flow rates in this experiment. Droplets in the channel width of 1.25pt were able to be formed in the water flow rate range of 1-8  $\mu\text{L}/\text{min}$  before stratification took place. The thinnest channel in this experiment (1pt line width) was able to form droplets from 2-6  $\mu\text{L}/\text{min}$ .  $Q_L = 7 \mu\text{L}/\text{min}$  saw stratification and 1  $\mu\text{L}/\text{min}$  was unable to consistently form droplets for the 1pt line width channel experiments. The flow regime switched between continuous flow and droplet generation. Figure 39 shows a fluctuating increase in droplet length as the water flow rate  $Q_L$  is increased in all three channel widths. Figure 40, Figure 41, and Figure 42 incorporate one standard deviation of the averaged droplet lengths for the three channel widths. Table 8 lists the experiment results. The fluctuation in trend is probably due to the channel roughness, water adherence to channel walls and pressure fluctuations as reported (Baroud, 2004; Tan, 2009). In trend, the wider the channel and higher the water flow rate, the longer the droplets.



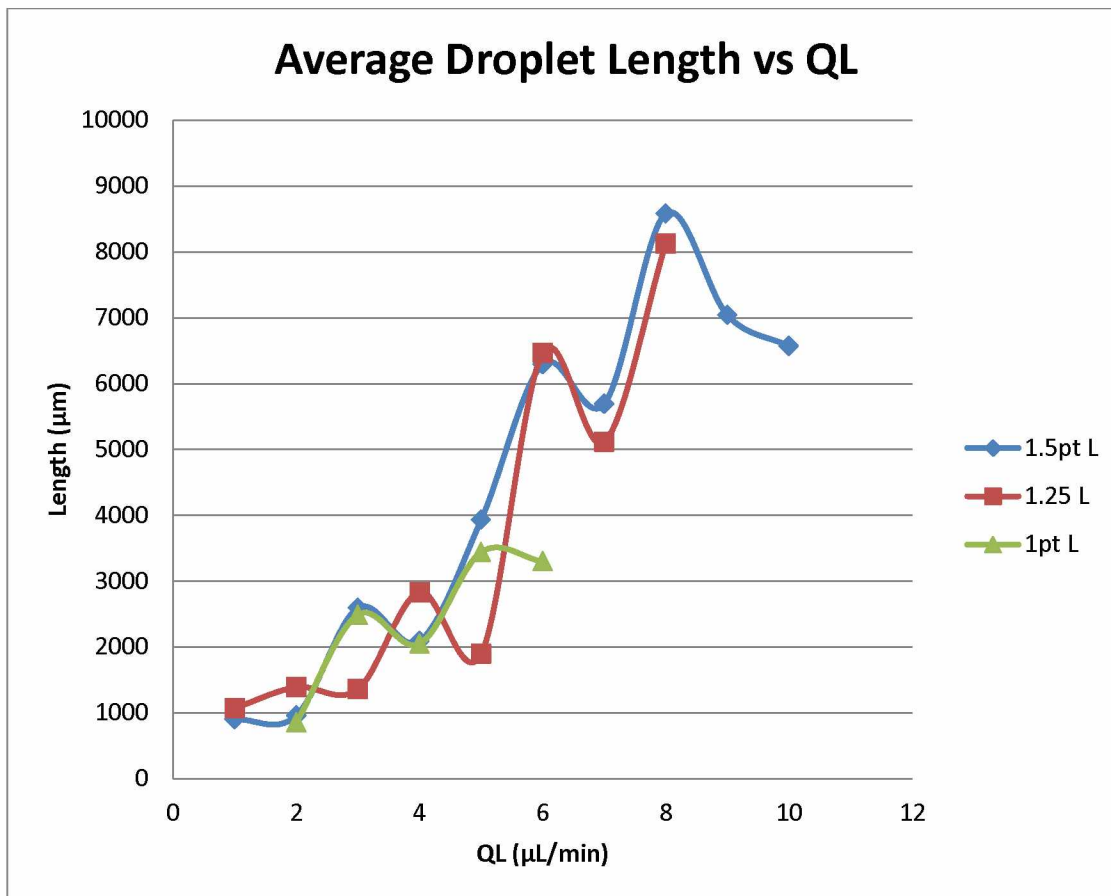


**Figure 39: Droplet length versus water flow rate. The pt size refers to the line width printed onto the thermalplastic sheet. 1.5pt has a channel width of 292µm, 1.25pt is 281µm, and 1pt is 258µm.**

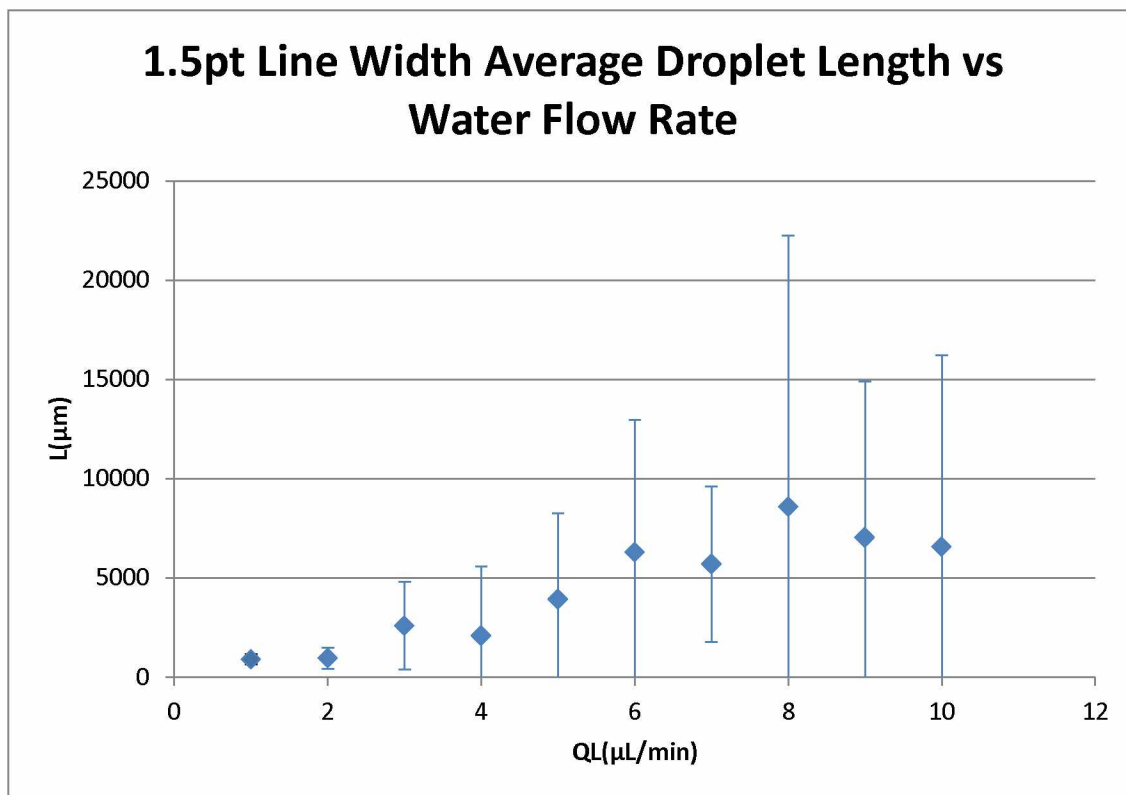


**Figure 40: Average droplet length versus water flow rate in the 1.5pt line width is depicted. One standard deviation of each average is incorporated into the graph.**

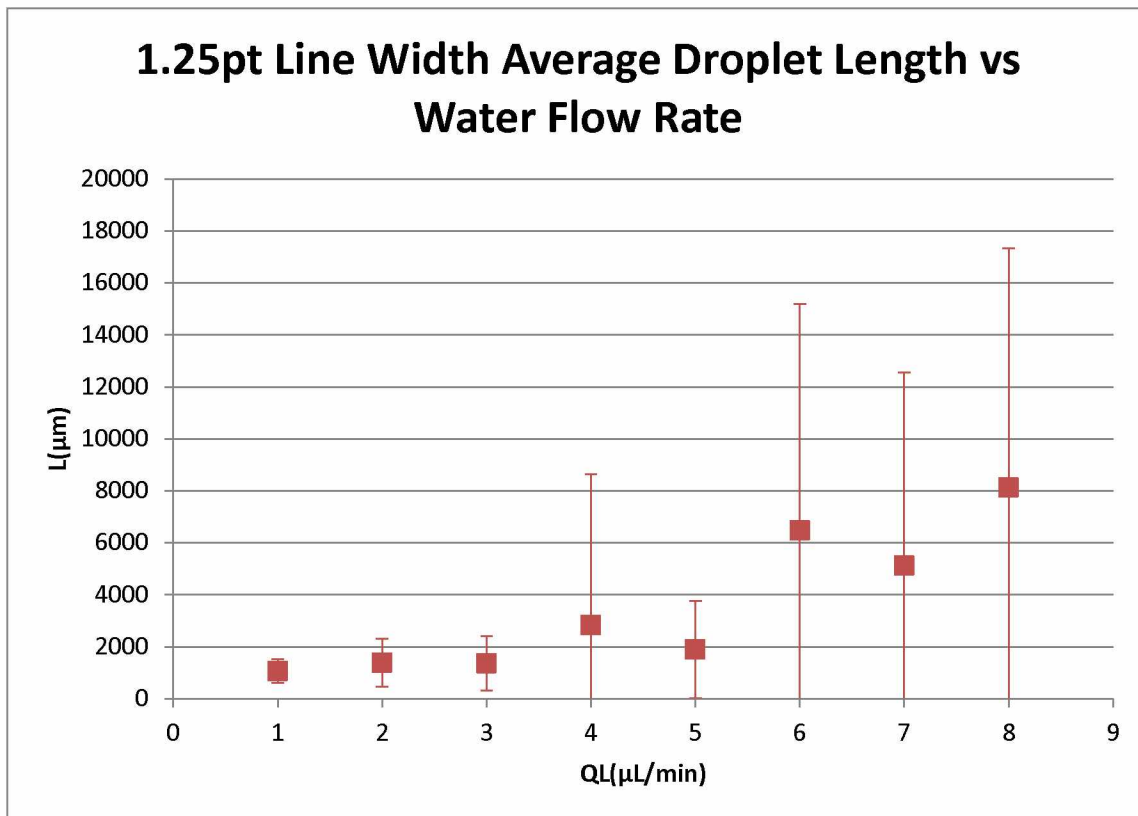


**Figure 41:** Average droplet length vs water flow rate in the 1.25pt line width is depicted. One standard deviation of each average is incorporated into the graph.

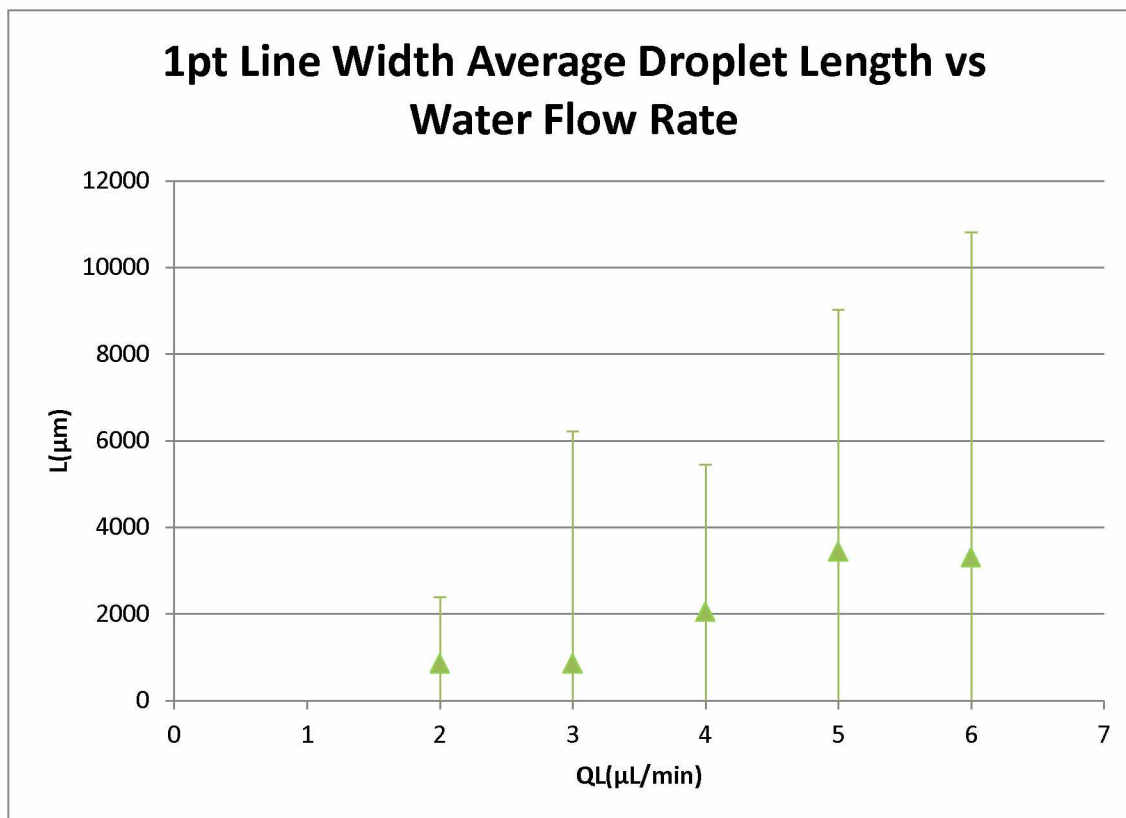


**Figure 42:** Average droplet length vs water flow rate in the 1pt line width is depicted. One standard deviation of each average is incorporated into the graph.

**Table 8: Droplet length versus liquid flow rate**

Line Width (pt)	$Q_L(\mu\text{L}/\text{min})$	$W(\mu\text{m})$	Average Droplet Length ( $\mu\text{m}$ )	STDEV of Average Length ( $\mu\text{m}$ )
1.5	1	292	900	255
1.5	2	292	957	527
1.5	3	292	2593	2208
1.5	4	292	2087	3491
1.5	5	292	3928	4345
1.5	6	292	6293	6670
1.5	7	292	5690	3918
1.5	8	292	8581	13682
1.5	9	292	7039	7850
1.5	10	292	6567	9644
1.25	1	281	1071	453
1.25	2	281	1389	932
1.25	3	281	1359	1045
1.25	4	281	2832	5816
1.25	5	281	1893	1878
1.25	6	281	6466	8730
1.25	7	281	5116	7426
1.25	8	281	8126	9211
1	2	258	852	1543
1	3	258	2489	5371
1	4	258	2046	3408
1	5	258	3439	5579
1	6	258	3297	7509

For 1.5pt line width (292  $\mu\text{m}$ ) the flow rate  $Q_L=2 \mu\text{L}/\text{min}$  has a slight increase in droplet length from  $Q_L=1 \mu\text{L}/\text{min}$ . One standard deviation at both of these flow rates appear to relatively small. There is a jump when  $Q_L=3 \mu\text{L}/\text{min}$  and almost a four-fold increase in standard deviation from the previous flow rate. The droplet length however is decreased

as  $Q_L$  is increased to  $4 \mu\text{L}/\text{min}$ , and the standard deviation raises approximately  $1190 \mu\text{m}$ . When the flow rate is raised to  $Q_L=5 \mu\text{L}/\text{min}$  there is a rise in droplet length as well as standard deviation. A steep rise occurs at  $Q_L=6 \mu\text{L}/\text{min}$  and with an apex at  $Q_L=8 \mu\text{L}/\text{min}$  with a slight drop in length at  $Q_L=7 \mu\text{L}/\text{min}$ . The flow rate  $Q_L=8 \mu\text{L}/\text{min}$  sees nearly a three and a half-fold increase in standard deviation from the previous flow rate. This shows that the droplet lengths vary greatly. The flow rates  $Q_L=9 \mu\text{L}/\text{min}$  and  $Q_L=10 \mu\text{L}/\text{min}$  show declines in droplet length and standard deviations from the  $Q_L=8 \mu\text{L}/\text{min}$  flow rate.

The line width  $1.25\text{pt}$  ( $281 \mu\text{m}$ ) follows a similar pattern to the  $1.5\text{pt}$  line width, but increases droplet size at  $Q_L=4 \mu\text{L}/\text{min}$ , and decreases at  $Q_L=3 \mu\text{L}/\text{min}$  and  $Q_L=5 \mu\text{L}/\text{min}$ .  $Q_L=8 \mu\text{L}/\text{min}$  was the highest flow rate for droplet production before stratification occurred. The standard deviations show an increasing trend except for a decrease at  $Q_L=5 \mu\text{L}/\text{min}$ .

The  $1\text{pt}$  line width ( $258 \mu\text{m}$ ) followed the trend of  $1.25\text{pt}$  with slightly lower velocities. The trend deviates at  $Q_L=6 \mu\text{L}/\text{min}$  and the average droplet length decreases by approximately  $140 \mu\text{m}$ . It should be noted that  $1\text{pt}$  line width has larger average droplet lengths at  $Q_L=3$  and  $5 \mu\text{L}/\text{min}$ , and  $1.25\text{pt}$  has larger average droplet lengths at  $Q_L=3, 5,$  and  $7 \mu\text{L}/\text{min}$  than the  $1.5\text{pt}$  line width. The droplet length standard deviations increase with increasing flow rate

### 5.3 Droplet Velocity Results

Due to the variations in the droplet lengths versus flow rates, the average droplet velocity was also examined. Figure 43 shows that the droplet velocity has a nearly inverse response to increasing the water flow rate in Figure 39. Table 9 lists the results. Once again 1.5pt and 1.25 follow similar trends. The graph shows that 1.5pt line width droplets have an increased velocity from  $Q_L=1 \mu\text{L}/\text{min}$  to  $Q_L=2 \mu\text{L}/\text{min}$  and a large decrease in velocity at  $Q_L=3 \mu\text{L}/\text{min}$ . A relatively small increase in velocity occurs at  $Q_L=4 \mu\text{L}/\text{min}$  and decreases in velocity are seen at  $Q_L=5 \mu\text{L}/\text{min}$  and  $Q_L=6 \mu\text{L}/\text{min}$ . Minor increases in droplet velocity occur at  $Q_L=7 \mu\text{L}/\text{min}$  and  $Q_L=10 \mu\text{L}/\text{min}$  and minute decreases occur at  $Q_L=8 \mu\text{L}/\text{min}$  and  $Q_L=9 \mu\text{L}/\text{min}$ .

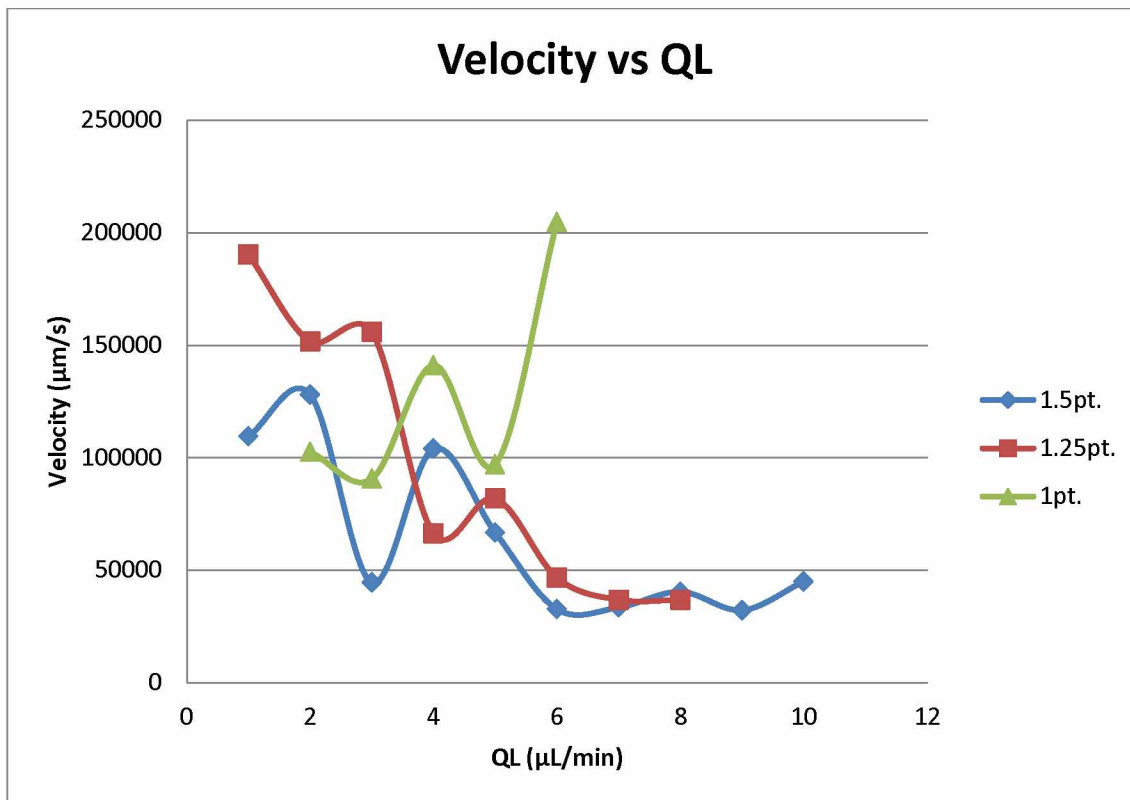


**Figure 43: Droplet velocity versus water flow rate. The pt. size refers to the line width printed onto the thermalplastic sheet. 1.5pt has a channel width of 292μm, 1.25pt is 281μm, and 1pt is 258μm.**

The line width 1.25pt declines from  $Q_L=1 \mu L/min$  to  $Q_L=2 \mu L/min$  with a slight increase in velocity at  $Q_L=3 \mu L/min$ . There is a large droplet velocity decrease at  $Q_L=4 \mu L/min$  and increases at  $Q_L=5 \mu L/min$ . Flow rates  $Q_L=6 \mu L/min$  and  $Q_L=7 \mu L/min$  have a decline in velocity versus flow rate. There is a small raise in velocity at  $Q_L=8 \mu L/min$ . The 1.25pt line width appears to have a higher average velocity than the 1.5pt from  $Q_L=1 \mu L/min$  to  $Q_L=3 \mu L/min$  and  $Q_L=5 \mu L/min$ .



**Table 9: Droplet average velocity versus water flow rate**

Line Width (pt)	QL( $\mu\text{L}/\text{min}$ )	W( $\mu\text{m}$ )	Average Droplet Velocity per Flow Rate ( $\mu\text{m}/\text{s}$ )	STDEV of Average Velocity per Flow Rate
1.5	1	292	109527	49067
1.5	2	292	127969	58084
1.5	3	292	44451	8124
1.5	4	292	103910	68957
1.5	5	292	66722	34895
1.5	6	292	32637	36083
1.5	7	292	33422	31240
1.5	8	292	40396	52492
1.5	9	292	32170	53497
1.5	10	292	44958	95436
1.25	1	281	190307	117202
1.25	2	281	151621	73399
1.25	3	281	155839	94352
1.25	4	281	66324	35923
1.25	5	281	81880	35908
1.25	6	281	46636	38394
1.25	7	281	36814	33567
1.25	8	281	36775	41621
1	2	258	102549	36521
1	3	258	90624	45443
1	4	258	141070	78229
1	5	258	96987	87452
1	6	258	204807	152259

The smallest channel width tested (1pt. printed line width) has an average velocity tendency to increase as water flow rates increase (see Table 9). The velocity drops from  $Q_L=2 \mu\text{L}/\text{min}$  to  $Q_L=3 \mu\text{L}/\text{min}$  with a decrease at  $Q_L=3 \mu\text{L}/\text{min}$ . There is an increase in

velocity at  $Q_L=4 \mu\text{L}/\text{min}$  followed by a decrease in velocity at  $Q_L=5 \mu\text{L}/\text{min}$  and a large increase at  $Q_L=6 \mu\text{L}/\text{min}$ .

Several factors are believed to contribute to the large inconsistencies in the average droplet lengths and velocities. It was noticed upon testing that some flow rates and devices exhibited a “dry” channel surface and other exhibited a “wet” channel surface (Figure 44 and Figure 45). The unwetted channel walls were noticed to produce droplets at slower speeds with more consistent lengths. This is believed to be due to the friction of the channel walls. The wall friction is consistent and will require more consistent pressures for droplet shearing. The wetting of the channel walls by water can enhance droplet shearing by reducing the friction in the channel. This is believed to cause smaller droplets that are less uniform. The friction in the channel is not uniform as the wet channel wall film was qualitatively observed to differ through the channels, thus requiring variations in pressure for droplet shearing. The wetting of the channel walls can also be seen to affect the contact angle of the droplets. In a study done by Choi (2008), different contact angles were studied numerically. The study found that the sliding and detachment of droplets were significantly dependent on the contact angle. The wet and dry channels varied through each line width and device, which may be a large contributor to the large standard deviations and trends with increasing water flow rates.

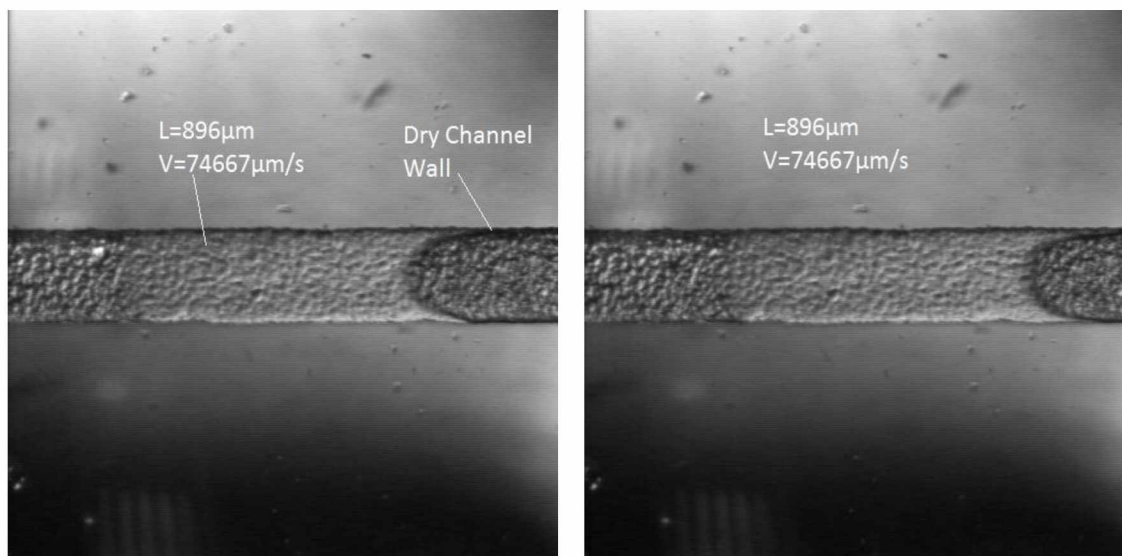


**Figure 44:** Example of consecutive droplets in dry channel. The droplets have the same length and velocities.

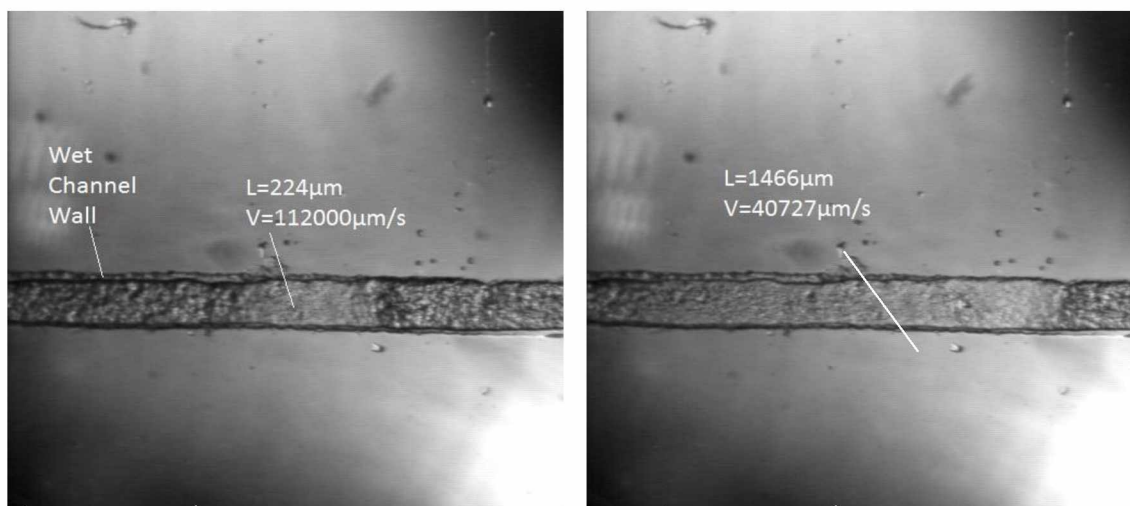


**Figure 45:** Example of consecutive droplets in wet channel. The droplets lengths and velocities differ.

It is not understood why some channels became wetted, while others remained dry. We think that plasma exposure may be part of it. Some post-plasma treated surfaces may have been exposed to the atmosphere longer than others, altering the hydrophobicity or hydrophilicity. Further investigation of the contact angles is suggested.

We also observed that there would be a few droplets produced at a relatively small and consistent length and velocity before a large droplet or continuous flow would proceed. There would be a pause in droplet production before the pressure would build up enough to produce the small consecutive droplets again. This phenomenon is thought to be due to the microsyringe pumps. These pumps are old and are screw driven. The threads may have blemishes that cause the pumps to pulse. Newer pumps that are not screw driven are recommended in future studies.

#### **5.4 Droplet Formation Mechanisms**

Droplet formation in PDMS channels can be affected by a few factors including the channel wall roughness, hydrophobicity treatment and the flow rates of the working fluids (Baroud, 2004). Further examinations of channel roughness, location of droplet formation, and variation in air flow rate were conducted in this section.

Channel roughness can increase undesired drag forces acting on the droplets causing reduced pressures, affecting velocities, and changing contact angles. Figure 46 shows the channel surface using a 25x achromat objective lense (Din standards Long Working Distance (LWD) objectives plan, N.A. 0.40, W.D. 4.8mm). The roughness is unavoidable in the fabrication process of the Shrinky Dinks® lithography. The channel effects are recommended as a future work.

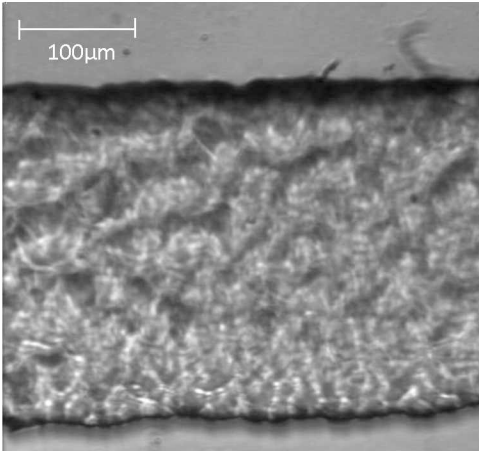


**Figure 46: Picture taken at 25x DIN LWD plan achromat objective, N.A. 0.40, W.D. 4.8mm.**

It also observed that droplets did not consistently form at the T-junction. A water “tail” developed trailing from the junction point sticking along one side of the channel downstream. A step by step process can be seen in Figure 47. It appears that air is being forced over the water tail and shearing the front face, rather than shearing at the base of the junction intersection.

A qualitative investigation of varying air rate was done to determine the effects of doubling and halving the air flow rate while maintaining the 30:1 air flow rate to water flow rate ratio. When the air flow rate was double a stratified flow regime occurred, as seen in Figure 48.

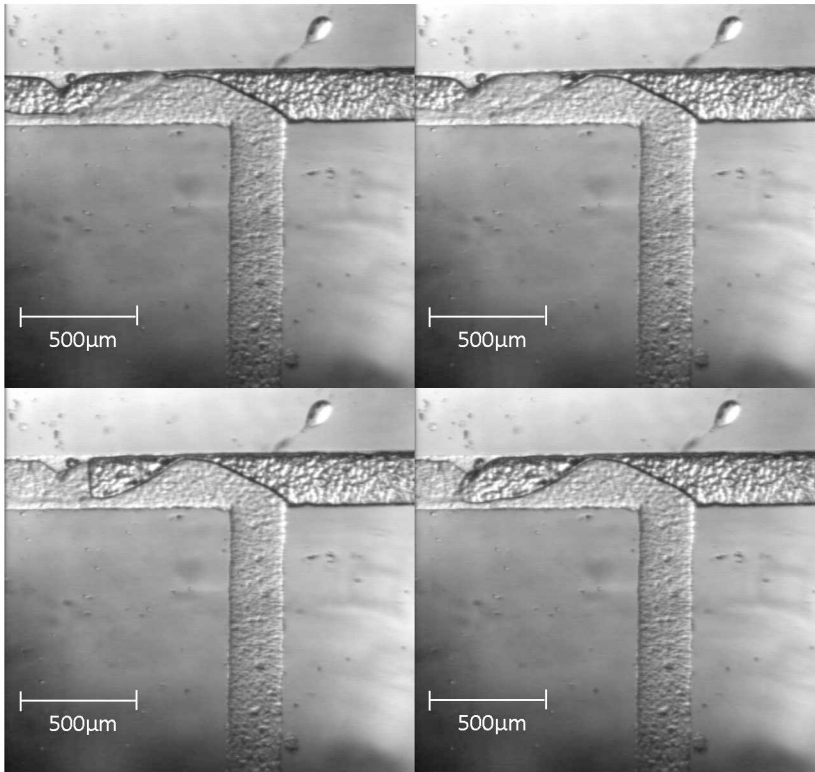


**Figure 47: Droplet formation at T-Junction. Top Left: droplet forming from water "tail." Top Right: Droplet interfacial stresses overtaking viscosity stresses. Bottom Left: Initial separation of droplet from water tail. Bottom right: Droplet separation from water tail. (The light gray area indicates the water phase, and the area with brighter dots is occupied by air).**

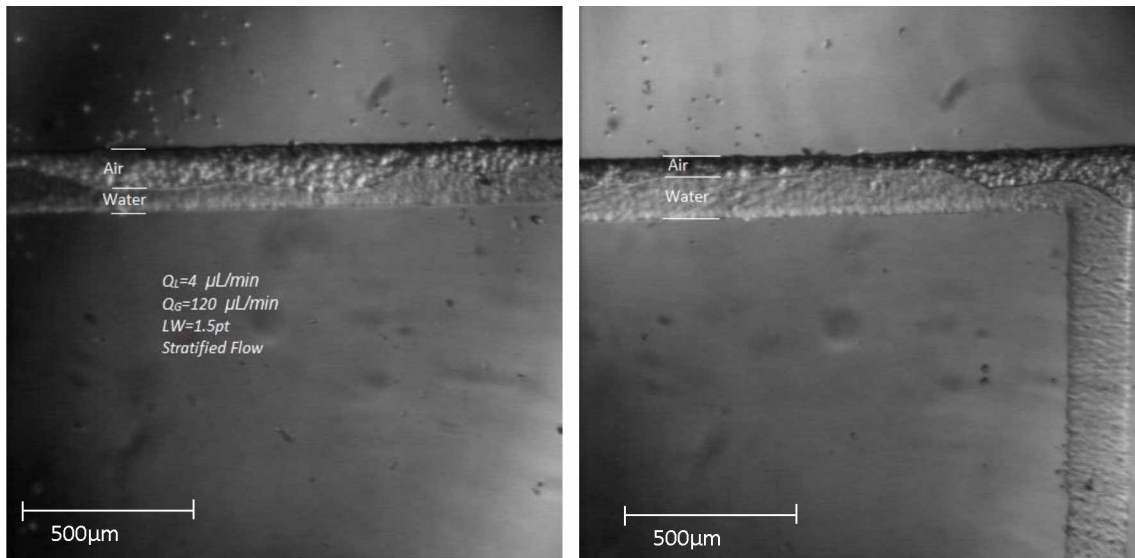


**Figure 48:  $Q_L=4 \mu\text{L}/\text{min}$ ,  $Q_G=120 \mu\text{L}/\text{min}$  in a 1.5pt lineweight channel. The water and air have become stratified. Left: Viewing window. Right: T-junction.**

At a high air flow rate of  $120 \mu\text{m}/\text{min}$  droplets were formed at the outlet hole, where the channel geometry experience a sudden change in dimension. This hole increased the channel width from  $292 \mu\text{m}$  to a diameter of  $7937.5 \mu\text{m}$ . The increase in channel dimensions helps reduce the surface curvature of the water and thus facilitates droplet breakup. The droplet production can be seen in Figure 49. The top left image shows a droplet being formed as the channel begins to widen. The image in the top right shows the area of the droplet thickening with water. The bottom left image shows the droplet shearing off and the bottom right shows the droplet fully separated from the continuous liquid flow.

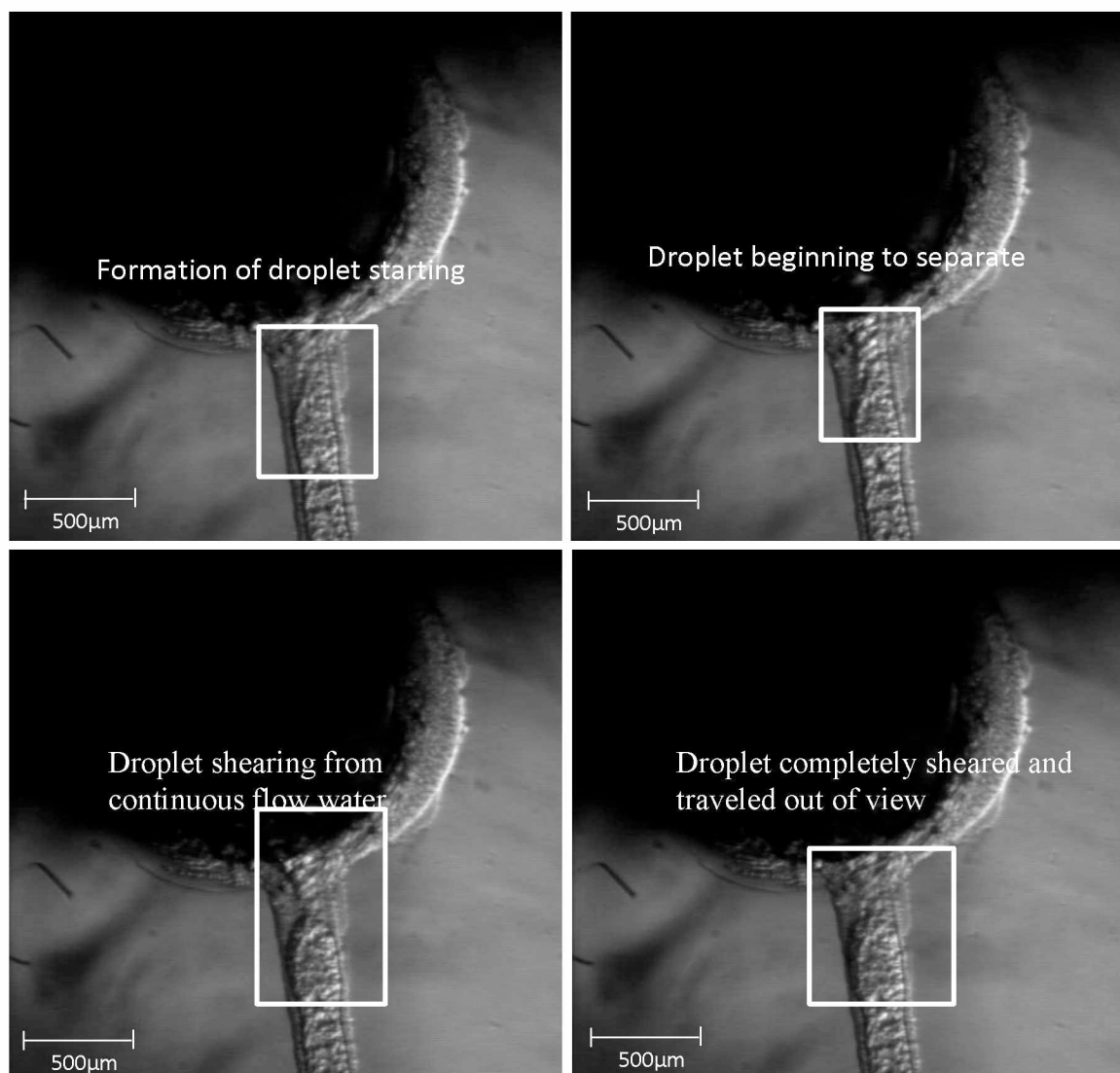
Images were taken of the outlet hose as the droplets were being produced at the outlet.

Figure 50 shows a droplet in the outlet hose. The expanding diameter of the hose created

short droplets. It is recommended that further investigation of outlet droplet formation be done.

When the air flow rate was halved, it was observed that droplet formation did not take place at the T-junction. Surface wetting created a water “tail” causing a liquid buildup approximately 3000  $\mu\text{m}$  from the T-junction (Figure 51). It can be seen that the water builds up at this point until the pressure is great enough to shear the accumulated water into a droplet. The water tail remains after the droplet shears leaving a wetted surface.





**Figure 49: Droplet formation at the outlet.**

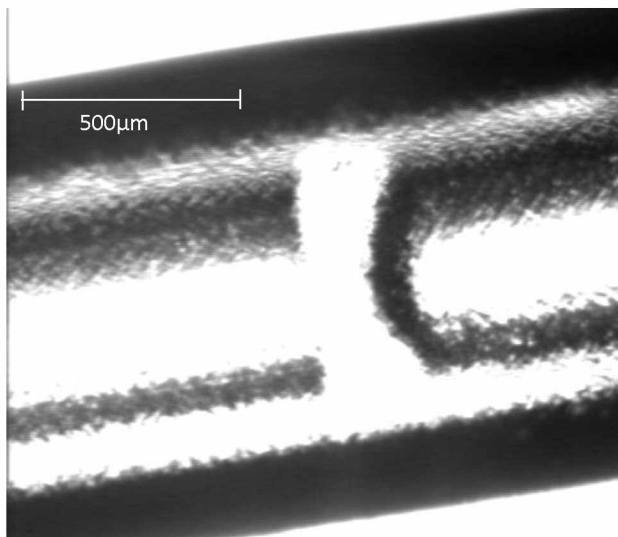


**Figure 50: Droplet formed in outlet. This picture is of the outlet hose with a droplet traveling through it.**

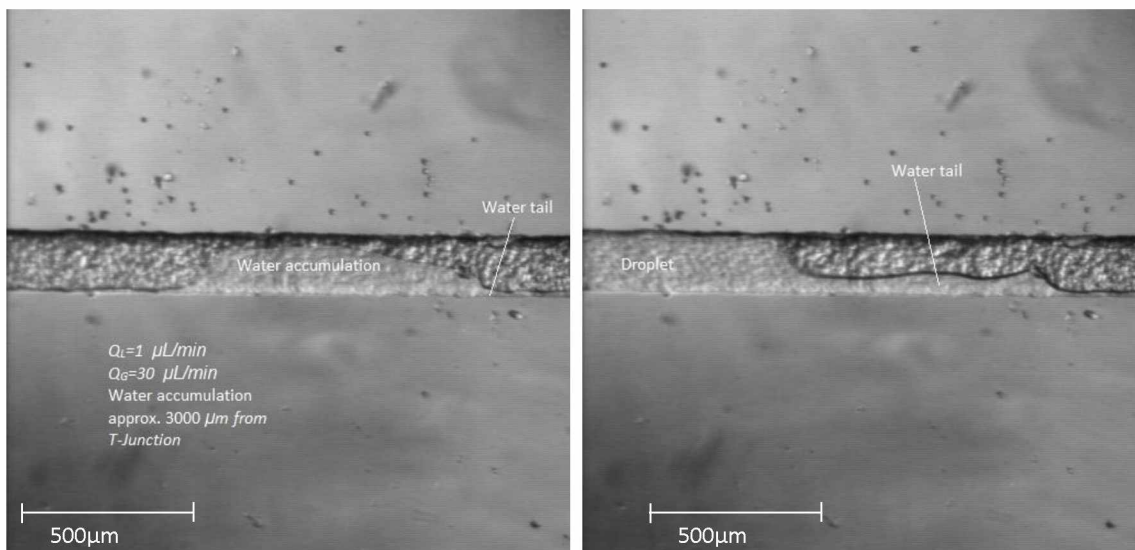


**Figure 51: Water accumulation creating droplets approximately 3000 μm from T-junction flowing right to left. Left: Water accumulation. Right: Droplet being formed from water accumulation on water tail when pressure becomes great enough to shear it. The product leaves the water tail.**

## 5.5 Chapter Conclusions

Two-layered PDMS devices were fabricated from thermalplastic (Shrinky Dinks®) sheets and plasma bonded. A T-junction geometry was used at the intersection. Air was injected in line with the channel and was the carrying fluid, while water was injected perpendicular to the channel. Water flow rates were increased from 1-10  $\mu\text{L}/\text{min}$  while keeping the air flow rate constant. Droplets in the line width of 1.5pt were able to be formed at all water flow rates. Droplets in the channel width of 1.25pt were able to be formed in the water flow rate range of 1-8  $\mu\text{L}/\text{min}$  before stratification took place. The thinnest channel in this experiment (1pt line width) was able to form droplets from 2-6  $\mu\text{L}/\text{min}$ .  $Q_L = 7 \mu\text{L}/\text{min}$  saw stratification and 1  $\mu\text{L}/\text{min}$  was unable to consistently form droplets. The flow regime switched between continuous flow and droplet generation.

Water-in-air microdroplets were formed without the use of surfactants or glycerol. An offset channel was implemented to aid in the separation of droplets in cases where water had built up along the channel wall. It was observed that droplet length increased and droplet velocity decreased non-uniformly over increasing flow rates. Reasons for this were investigated and thought to be due to surface roughness of the channel, pressure fluctuations, and water adherence to the channel walls.

It was observed that at a doubled air flow rate, with a 30:1 air to water ratio, droplets were not produced until the stratified flow reached the geometric expansion of the channel outlet. Uniform droplets were then produced in the outlet hose.

When the air flow rate was halved, maintaining the 30:1 ratio, droplets were observed to not form at the T-junction, but rather 3000  $\mu\text{m}$  down where a water “tail” had accumulated enough to block the air flow. The air flow would then build up enough pressure to shear a droplet from this accumulation from the front face by, essentially, pushing the top of the accumulated water down the channel, rather than from the base of the built up fluid.

## Chapter 6 Summaries and Future Work

### 6.1 Summaries of Chapter Conclusions

Twenty four samples were created using two-layered PDMS substrates to test the bonding strength by air plasma, which is governed by three control variables: the time, RF (power input), and vacuum chamber pressure were all altered to determine the optimal combination of these variables for further testing in microdroplet formation. The first trial was subjected to a manual peel test to identify the percentage of the surface was bonded. Due to the peel test and time reduction being an optimal variable, the bonding parameters of 30 second bond time (with an added 15 second plasma warm up time) at medium (10.5W) radio frequency, and 200mTorr chamber pressure were used in the microfluidic trials. It was observed that unfiltered air plasma assisted PDMS-PDMS bonds with these settings could withstand 135 psi (930 kPa).

Two-layered PDMS devices were fabricated from thermalplastic sheets and plasma bonded. A T-junction geometry was used at the intersection. Air was injected in line with the channel and was the carrying fluid, while water was injected perpendicular to the channel. Water-in-air microdroplets were formed without the use of surfactants or glycerol. An offset channel was implemented to aid in the separation of droplets in cases where water had built up along the channel wall. It was observed that droplet length increased and droplet velocity decreased non-uniformly over increasing flow rates. Reasons for this were investigated and thought to be due to surface roughness of the channel, pressure fluctuations, and water adherence to the channel walls.

## 6.2 Future Work

- Investigation into thinner channels is recommended to determine if channel width effects droplet shearing at the T-junction.
- Using a resolution higher than 1200 dpi may reduce surface roughness in the channels.
- The variation in droplet length and velocity may be due to the pressure driven micropumps that were used in this experiment. They are driven by a large screw, which has a tendency to pulse. Harvard Apparatus has produced a pump that avoids this method of fluid propulsion.
- Varying gas flow rates may be used to optimize droplet length and production rate. It was observed that droplets were formed in the outlet, flowing into the exiting hose. This hose transported uniform length droplets, which may provide transporting methods from device to device.
- Geometry manipulation may provide assistance in controlled droplet production. Widening the channels will reduce the velocity and interfacial tension in the droplet, creating droplets more readily.
- Further study into the effects of the offset channel should be conducted. The effects of droplet shearing were not compared to that of an aligned channel when entering the first curve from the T-junction.
- The use of surfactants should be investigated to improve droplet uniformity and stabilization. The surfactants have proven to reduce water buildup on the channels by creating a hydrophilic surface.

- Studying droplet contact angles at the leading and trailing edges should be done.

It was quantitatively observed that the leading edge did not take on a convex shape while the pressure driven trailing end did.

## References

- Baroud, C. N. (2004). Multiphase Flows in Microfluidics. (Elsevier, Ed.) *Comptes Rendus Physique*, 547-555.
- Bhattacharya, S. D. (2005). Studies on Surface Wettability of Poly(dimethyl)siloxane (PDMS) and Glass Under Oxygen-Plasma Treatment and Correlation with Bond Strength. *J. Microelectromech. Syst.*, 590-7.
- Brouzes, E. M. (2009). Droplet Microfluidic Technology for Single-Cell High-Throughput Screening. *Proceedings of National Academy of Science*, 106(34), 14195-14200.
- Chen, C. D. (2008). Droplet-Based Microdialysis-Concept, Theory, and Design Considerations. *Journal of Chromatography A*, 29-36.
- Chen, C. (n.d.). Lecture Notes of ME 640, Introduction to Microfluidics. University of Alaska Fairbanks.
- Cheow, L. F. (2007). Digital Microfluidics: Droplet Based Logic Gates. *Appl. Phys. Lett.*
- Choi, J. S. (2008). Numerical Study of Droplet Motion in a Microchannel with Different Contact Angles. *Journal of Mechanical Science and Technology*, 2590-2599.
- Chueh, B. H. (2007, May 1). Leakage-Free Bonding of Porous Membranes into Layered Microfluidic Array Systems. *National Institute of Health Public Access-Author Manuscript*, 79(9), 3504-3508.
- Dow Corning Corporation. (2011). *Sylgard 184 Silicone Elastomer Kit*. Retrieved May 26, 2011, from <http://www.dowcorning.com/applications/search/products/Details.aspx?prod=01064291&type=PROD>
- Drew, K. P. (2004). Sampling Glutamate and GABA with Microdialysis: Suggestions on how to get the dialysis membrane closer to the synapse. *Journal of Neuroscience Methods*, 127-131.
- Dreyfus, R. T. (2003). Ordered and Disordered Patterns in Two Phase Flows in Microchannels. *Phys. Rev. Lett*, 90.
- Duffy, D. M. (1998). Rapid Prototyping of Microfluidic Systems in Poly(dimethylsiloxane). *Anal Chem.*, 70, 4974-4984.



- Eddings, M. A. (2008). Determining the Optimal PDMS-PDMS Bonding Technique for Microfluidic Devices. *Journal of Micromechanics and Microengineering*(18), 1-4.
- Franks, M. (2008). *Fabrication of Microfluidic Channels, Final Report of ME 487 Senior Design Projects*. University of Alaska Fairbanks.
- Fuerstman, M. J. (2007). Coding/Decoding and Reversibility of Droplet Trains in Microfluidic Networks. *Science*, 828-832.
- Gershenfeld, P. (2007). Microfluidic Bubble Logic. *Science*, 832-835.
- Grimes, A. B. (2008). Shrinky-Dink Microfluidics: Rapid Generation of Deep and Rounded Patterns. *Lab on a Chip*.
- Harrick Plasma. (n.d.). *Plasma Products: Plasma Cleaners*. Retrieved from [http://www.harrickplasma.com/products\\_cleaners.php](http://www.harrickplasma.com/products_cleaners.php)
- Harris, J. L. (2007). Non-plasma Bonding of PDMS for Inexpensive Fabrication of Microfluidic Devices. (9).
- Haubert, K. D. (2006, October 19). PDMS bonding by means of a portable, low-cost corona system. *Royal Society of Chemistry*.
- K & B Innovations, I. U. (2010). *The Magical World of Shrinky Dinks*. Retrieved July 13, 2011, from <http://www.shrinkydinks.com/>
- Manz, A. G. (1990). Contactless Electrochemical Actuator for Microfluidic Dosing. *Journal of Microelectromechanical Systems*, 244-248.
- Middelstat, N. M. (2010). *PDMS Fabrication Manual, Final Report of ME 487 Senior Design Projects*. Fairbanks.
- Plasma & Plasma Cleaning*. (n.d.). Retrieved 03 12, 2011, from <http://www.bitu.lu/datasheets/Plasma-PlasmaCleaning-S.pdf>
- Tan, J. L. (2009). Gas-Liquid Flow in T-Junction Microfluidic Devices With a New Perpendicular Rupturing Flow Route. *Chemical Engineering Journal*, 428-433.
- Tan, Y. C. (2005, July 26). Monodispersed Microfluidic Droplet Generation by Shear Focusing Microfluidic Device. *Science Direct*, 350-356.

- Tang, K. C. (2006). Evaluation of bonding between oxygen plasma treated polydimethyl siloxane and passivated silicon. *Journal of Physics, Conference Series*(34), 155-161.
- Teh, S. L. (2008, January 11). Droplet Microfluidics. *Royal Society of Chemistry*, 8, 198-220.
- Triplett, K. G.-K. (1999). Gas-Liquid Two-Phase Flow in Microchannels. Part I: Two-Phase Flow Patters. *Int. J. Multiphase Flow*, 377-394.
- van Midwoud, P. M. (2010, January 1). Microfluidic Biochip for the Perifusion of Precision-Cut Rat Liver Slices for Metabolism and Toxicology Studies. *Biotechnology and Bioengineering*, 105(1), 184-194.
- White, R. N. (2007). *PDMS-Glass Bonding via Oxygen Plasma*. March Plasma.
- Xia, Y. W. (1998). Soft Lithography. *Angew. Chem. Int.*, 550-575.
- Yobas, L. M. (2006). High-Performance Flow-Focusing Geometry for Spontaneous Generation of Monodispersed Droplets. *Lab on a Chip*, 1073-1079.